Langmuir Probe Measurements in the Plume of a Pulsed Plasma Thruster

by

Lawrence Thomas Byrne

A Thesis

Submitted to the Faculty

of the

WORCESTER POLYTECHNIC INSTITUTE

in partial fulfillment of the requirements for the

Degree of Master of Science

in

Mechanical Engineering

November 2002

APPROVED:

_____
Dr. Nikolaos A. Gatsonis, Advisor
Associate Professor, Mechanical Engineering Department

_____
Dr. John Blandino, Committee Member
Assistant Professor, Mechanical Engineering Department

_____
Dr. David Olinger Committee Member
Associate Professor, Mechanical Engineering Department

_____
Eric Pencil, Committee Member
NASA Glenn Research Center

_____
Dr. Michael Demetriou, Graduate Committee Representative
Assistant Professor, Mechanical Engineering Department

Abstract

The ablative Teflon pulsed plasma thruster (PPT) is an onboard electromagnetic propulsion enabling technology for small spacecraft missions. The integration of PPTs onboard spacecraft requires the understanding and evaluation of possible thruster/spacecraft interactions. To aid in this effort the work presented in this thesis is directed towards the development and application of Langmuir probe techniques for use in the plume of PPTs. Double and triple Langmuir probes were developed and used to measure electron temperature and density of the PPT plume. The PPT used in this thesis was a laboratory model parallel plate ablative Teflon® PPT similar in size to the Earth Observing (EO-1) PPT operating in discharge energies between 5 and 40 Joules.

The triple Langmuir probe was operated in the current-mode technique that requires biasing all three electrodes and measuring the resulting probe currents. This new implementation differs from the traditional voltage-mode technique that keeps one probe floating and requires a voltage measurement that is often susceptible to noise in the fluctuating PPT plume environment. The triple Langmuir probe theory developed in this work incorporates Laframboise's current collection model for Debye length to probe radius ratios less than 100 in order to account for sheath expansion effects on ion collection, and incorporates the thin-sheath current collection model for Debye length to probe radius ratios greater than 100. Error analysis of the non-linear system of current collection equations that describe the operation of the current-mode triple Langmuir probe is performed as well.

Measurements were taken at three radial locations, 5, 10, and 15 cm from the Teflon® surface of the PPT and at angles of 20 and 40 degrees to either side of the

thruster centerline as well as at the centerline. These measurements were taken on two orthogonal planes, parallel and perpendicular to the PPT electrodes. A data-processing software was developed and implements the current–mode triple Langmuir probe theory and associated error analysis. Results show the time evolution of the electron temperature and density. Characteristic to all the data is the presence of hot electrons of approximately 5 to 10 eV at the beginning of the pulse, occurring near the peak of the discharge current. The electron temperature quickly drops off from its peak values to 1-2 eV for the remainder of the pulse. Peak electron densities occur after the peak temperatures. The maximum electron density values on the centerline of the plume of a laboratory PPT 10 cm from the Teflon® surface are $6.6 \times 10^{19} \pm 1.3 \times 10^{19}$ m^{-3} for the 5 J PPT, $7.2 \times 10^{20} \pm 1.4 \times 10^{20}$ m^{-3} for the 20 J PPT, and $1.2 \times 10^{21} \pm 2.7 \times 10^{20}$ m^{-3} for the 40 J PPT. Results from the double Langmuir probe taken at $r = 10\,\text{cm}, \theta_{\perp} = 70°\,\text{and}\,90°$ of a laboratory PPT showed good agreement with the triple probe method.

Acknowledgements

I would like to express my sincere thanks and gratitude to everyone that helped to make this thesis and my education at WPI possible. I'd like to acknowledge the undergraduate students who assisted me as part of their major qualifying project in the design and fabrication of this experiment, Jeff Hammel, Matt Krumanaker, Jurg Zwahlen, Hilary Seling, and Adrian Wheelock. Their help and companionship in Cleveland were essential.

A large debt of gratitude is owed to Eric Pencil of NASA Glenn Research Center for making this research possible and allowing the use of NASA's facilities. His constant encouragement and patience in putting up with all of my questions was wonderful. To Lynn Arrington, Luis Pinero, and Tom Haag of NASA, thank you for all your technical assistance. And especially Mike Swiatek and Jim Nichols for all their hard work keeping CW-19 up and running for me. My gratitude to Hani Kamhawi of NASA in all his help and assistance can't be mentioned enough.

I can't thank Jurg and Adrian enough for all the time they spent on the code. All those hours spent chasing down errors won't go unappreciated.

Most of all I'd like to thank my advisor Professor Nikos Gatsonis for all his help and inspiration. His advice and insight have been invaluable throughout my entire time in his CGPL lab.

Of course I can't forget my friend and future wife, Rebecca Prince. Without her help and support this thesis would have dragged on forever.

Finally I'd like to acknowledge the funding that made this all possible. It was provided both by a NASA Massachusetts Space Grant Consortium fellowship and by NASA grant NAG3-2405.

Table of Contents

List of Figures

List of Tables

Nomenclature

A_p	=	area of probe $p=1,\ 2,\ 3$
$\overline{C}_i$	=	most probable ion speed
C^+	=	carbon ion
F^+	=	fluorine ion
d_s	=	probe sheath thickness
e	=	electron charge
eV	=	electron-volt
$f_{e(i)}(\mathbf{r},\mathbf{v},t)$	=	electron (ion) distribution function
g_0	=	gravitational acceleration at sea level
I_D	=	discharge current
I_p	=	current of probe $p=1,\ 2,\ 3$
$I^*_{e(i)}$	=	electron (ion) saturation current
$I_{e(i)}$	=	electron (ion) current
I_{sp}	=	specific impulse
$J^*_{e(i)}$	=	electron (ion) saturation current density
J_e	=	electron current density
J_{e0}	=	random electron thermal current density
J_i	=	ion current density
J_{i0}	=	random ion thermal current density
Kn_{st}	=	Knudsen number for s-t collisions
k	=	Boltzmann's constant
L_p	=	probe length
$m_{i(e)}$	=	mass of ion (electron)
N	=	number of samples
$n_e(r,\theta,t)$	=	electron number density
$n_e^{\max}(r,\theta)$	=	maximum electron density during a pulse
n_i	=	ion number density
r	=	radial distance downstream from the center of the Teflon® surface
r_p	=	probe radius
s	=	probe spacing
S_ϕ	=	standard deviation of probe potential
T	=	thrust
$T_e(r,\theta,t)$	=	electron temperature
$T_e^{\max}(r,\theta)$	=	maximum electron temperature

T_i	=	ion temperature
t	=	time
$U_{i(e)}$	=	ion (electron) drift velocity
α	=	Peterson-Talbot curve fit parameter
β	=	parameter that characterizes variation of ion current with probe potential
χ_p	=	nondimensional potential at probe $p=1,\ 2,\ 3$
ε_0	=	permittivity of free space
$\overline{\phi}$	=	mean probe potential
ϕ_b	=	double Langmuir probe bias potential
ϕ_f	=	floating potential
ϕ_p	=	probe potential $p=1,\ 2,\ 3$
ϕ_s	=	space potential
ϕ_{sp}	=	potential difference between space and probe
ϕ_{pp}	=	potential difference between two probes
λ_D	=	Debye length
λ_{st}	=	mean free path for collisions between species s and t
$\theta_{\perp(\parallel)}$	=	perpendicular (parallel) plane polar angle measured from the center of the Teflon® surface
τ_L	=	probe end-effect parameter

Chapter 1 Introduction

Electric propulsion (EP) is a means of spacecraft propulsion that uses electrical energy to produce thrust as opposed to chemical energy used in chemical propulsion. There are three distinct types of EP devices: electrothermal, electrostatic, and electromagnetic. One measure of efficiency of a propulsion device is its specific impulse (I_{sp}). The ratio of thrust produced over the weight flow rate of propellant mass expended, $I_{sp} = \frac{T}{\dot{m} g_o}$. The higher the I_{sp} of a particular engine the more efficient it is. Electrothermal thrusters use electrical energy to heat a propellant that then expands through a nozzle producing thrust. An example is a resistojet with a typical $I_{sp} \sim 300$ s and the arcjet with typical $I_{sp} \sim 400$ - 800 s. Electrostatic thrusters use electrostatic fields to accelerate a charged propellant. An example is the ion engine with typical $I_{sp} >2500$ s. The third type of EP device is electromagnetic and uses both electric and magnetic fields that are used to accelerate ionized gases. The PPT with a typical $I_{sp} \sim 800$ - 1200 s and the Hall thruster with typical $I_{sp} >1600$ s are examples of electromagnetic thruster. Table 1.1 shows typical performance characteristics of several EP thrusters.

Table 1.1 Characteristics of selected electric propulsion flight systems, [adapted from Sackheim and Byers, 1998].

Concept	Specific Impulse, s	Input Power, kW	Thrust/power, mN/kW	Specific Mass, kg/kW	Propellant
Resistojet	296	0.5	743	1.6	N_2H_4
	299	0.9	905	1	N_2H_4
Arcjet	480	0.85	135	3.5	NH_3
	502	1.8	138	3.1	N_2H_4
	>580	2.17	113	2.5	N_2H_4
	800	26	------	------	NH_3
PPT	847	<0.03	20.8	195	Teflon®
	1200	<0.02	16.1	85	Teflon®
Hall	1600	1.5	55	7	Xenon
	1638	1.4	------	------	Xenon
	2042	4.5	55.3	6	Xenon
Ion	2585	0.5	35.6	23.6	Xenon
	2906	0.74	37.3	22	Xenon
	3250	0.6	30	25	Xenon
	3280	2.5	41	9.1	Xenon
	3400	0.6	25.6	23.7	Xenon

With an I_{sp} on the order of a 1000 s and up, EP devices are significantly more efficient than chemical thrusters that typically achieve specific impulses of less than 500 s. This means that the propellant mass of an EP device that is needed to accomplish a given change in velocity of a satellite is much less than with a chemical device.

$$\Delta V = g_0 I_{sp} \ln\left(\frac{M_o}{M_f}\right) \tag{1.1}$$

Where g_0 is gravitational acceleration at sea level and M_o is the wet mass of the vehicle (includes all propellant) and M_f is the dry mass of the vehicle. Propulsion options that use fuel as efficiently as possible while taking up as little mass as possible are in high demand. A reduction in propellant mass translates into a larger payload capacity,

increased mission capability, and/or reduced launch vehicle costs. This is where electric propulsion becomes a viable alternative.

The increased efficiency of EP devices (high I_{sp}) comes at the expense of thrust produced. Thrust is limited by the amount of power available onboard. Typically, EP devices achieve thrust levels on the order of milli-newtons as shown in Table 1.1. Thus making EP devices ill suited for high thrust tasks such as launch vehicles or for a task that requires a rapid change in velocity. EP devices are extremely effective at orbit raising over long periods of time. They also are well suited for station keeping and precision pointing of satellites. Part of the current trend in the spacecraft industry is towards constellations of small satellites. The ability to scale down EP devices makes them invaluable for use with small satellites. EP can be used and is very effective on large space craft as well.

The particular EP device being investigated in this thesis is a pulsed plasma thruster (PPT). A PPT is a type of electromagnetic propulsion device that ablates, ionizes and then accelerates a solid Teflon® propellant to generate thrust. There are two basic types of PPTs, the gas-fed and the ablative. They both operate in a similar fashion their difference lying in the type of propellant used. The gas-fed PPT uses a gaseous propellant typically Xenon, while the ablative PPT uses a solid substance as propellant, typically Teflon®. The two types of PPT have been both operated in a rectangular electrode arrangement as well as a coaxial electrode arrangement. A new variant of the PPT is the micro-PPT. The micro-PPT is defined as having electrode spacing on the order of millimeters or less. The PPT used in this thesis is a rectangular geometry ablative type using Teflon®, shown in Figure 1.1. It consists of a pair of parallel plate

electrodes with the Teflon® propellant located between the electrodes. A spark initiating device (sparkplug) is located near the base of the electrodes embedded within the cathode. A capacitor is placed across the electrodes and charged to potential of ~1500 V. The discharge is initiated by firing the sparkplug, emitting electrons that create a path for a surface discharge of the capacitor across the Teflon® propellant face. This discharge ablates and ionizes several micrograms of the Teflon® surface. The current flowing between the electrodes creates a self-induced magnetic field orthogonal to the current vector. The acceleration of the ions is accomplished through the Lorentz force $(\mathbf{F} = \mathbf{J} \times \mathbf{B})$ that is directed out of the thruster parallel to the electrodes. A portion of the ablated Teflon® is not ionized; this neutral gas is pushed out of the thruster channel by gas dynamic effects [Vondra et al., 1970]. As the Teflon® propellant is ablated, a feed spring pushes it forward.

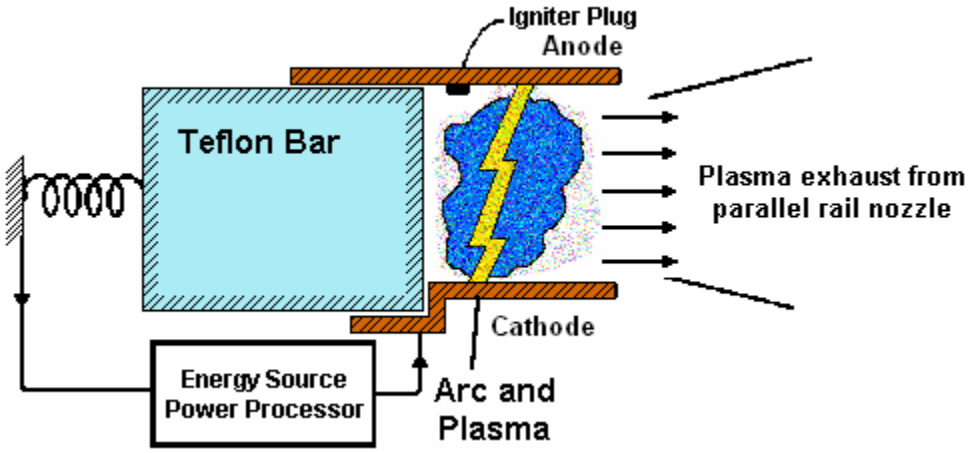

Figure 1.1 Diagram of ablative parallel plate PPT.

The attractive features of a PPT are its lack of moving parts, small volume, and use of solid propellant. The only moving part in a typical PPT is a feed spring for the propellant bar. The solid propellant significantly reduces the mass and volume required of a PPT system by eliminating the propellant tanks and valves. This significantly increases the reliability of the PPT system as well as providing a significant cost savings both in design and spacecraft integration.

The PPT offers many desirable performance abilities as well. Power throttling of the PPT can be achieved over a wide range without a thrust performance loss by varying the pulse repetition rate or varying the pulse energy [Sankovic and Dunning, 1999; Benson et al., 1999]. Most solid propellant PPTs operate at average power levels of 1 W – 200 W with specific impulses over 1000 s. The PPTs impulse bit (typically 25 μN-s – 2 mN-s) allows for very fine control of spacecraft.

Flight PPT systems were developed and flown between 1964 and 1982 [Myers et al., 1994]. The most notable flight applications were the Russian Zond-2 interplanetary probe, and in the U.S. the LES-6 and TIP/NOVA spacecraft [Meckel et al., 1996]. In the recent past the Japanese flew a PPT on the ETS-IV test satellite in 1982. The PPT was used for station keeping on all of these satellites. The small impulse bit of the PPT makes it well suited for this type of application. These flights occurred in the late 1960's through the 1970's. The development of the PPT came to a stop in the early 1980's when the trend in spacecraft was moving towards large very high power satellites. The power requirement for a PPT to be effective on these types of satellites was impractical as no power would be available for anything but propulsion.

The current emphasis in the spacecraft community is cost reduction. One of the ways to accomplish this is through multiple small spacecraft performing part of or all of the role of one large spacecraft. These smaller spacecraft can be launched as secondary payloads on launch vehicles or on a smaller launch vehicle for significant cost savings. For small spacecraft to be functional a reduction in the various subsystem masses is also necessary. The simplicity of the PPT and its small mass has brought renewed interest to the PPT, as it offers a simple bolt on package requiring only a few electrical connections. Another trend is towards constellations of small satellites to be used for communication and imaging/interferometry missions. The ability of the PPT to apply a very small impulse bit makes it ideal for the precision station keeping that will be necessary to maintain these constellations. The Air Force's TechSat 21 mission is an example of a formation-flying mission involving three satellites that will use PPTs [Spores and Birkan, 1999].

The first use of a PPT since the 1980's in space was flown on NASA's EO-1 satellite. It was launched on November 21, 2000 and successfully operated the PPT in 2002 [Zakrzwski et al. 2002]. This mission was designed to be a technology demonstrator for advanced technologies, among them a PPT developed by Primex (now AeroJet) and NASA GRC [Benson et al, 1999]. This will be the first on-orbit demonstration of a low mass, low cost, dependable electromagnetic PPT propulsion unit for precision attitude control. The PPT will be used at the end of the mission to replace one of the momentum wheels for attitude control. Three primary functions were performed by the PPT during its mission:

1 Counter environmental torques by firing at low energy levels.

2 Manage momentum while solar arrays are being rewound. PPT will fire at intermediate energy levels (8.5 – 56-J).

3 Manage momentum during specific science events that require solar arrays to be retracted and then deployed. The PPT will operate at a high energy level.

The PPT will demonstrate its ability to perform precision attitude control by conducting a series of fine pitch pointing maneuvers. The thruster being used has a specific impulse of 900-1200 s, an impulse bit of 10-1000 μN-s, and a scaleable average power of <1 to 100 W.

As with any onboard propulsion technology integration of PPTs requires the assessment of possible plume/spacecraft interactions. The exhaust plume of a PPT is a dense mixture of electrons, neutrals, and ions from the decomposition of the Teflon® polymer (Figure 1.2). Material sputtered from the electrodes, sparkplug, and nozzle are contained within the plume as well. The plume is primarily composed of slow moving neutrals and fast moving charged particles (ions/electrons). There also exist particles that result from charge exchange collisions taking place which give off fast moving neutrals and slow moving ions with a strong potential for backflow. One of the concerns spacecraft designers have is possible impingement of plume particles onto spacecraft surfaces or sensitive scientific instruments. Concern has also been expressed as to the existence of electromagnetic interference from the arc discharge of the PPT and its exhaust. The gigahertz radiation emitted from the spark igniter could possibly interfere with primary transceiver frequencies and the megahertz EMI radiation from the main PPT discharge could interfere with the radar frequency shifts [Spores and Birkan, 1999].

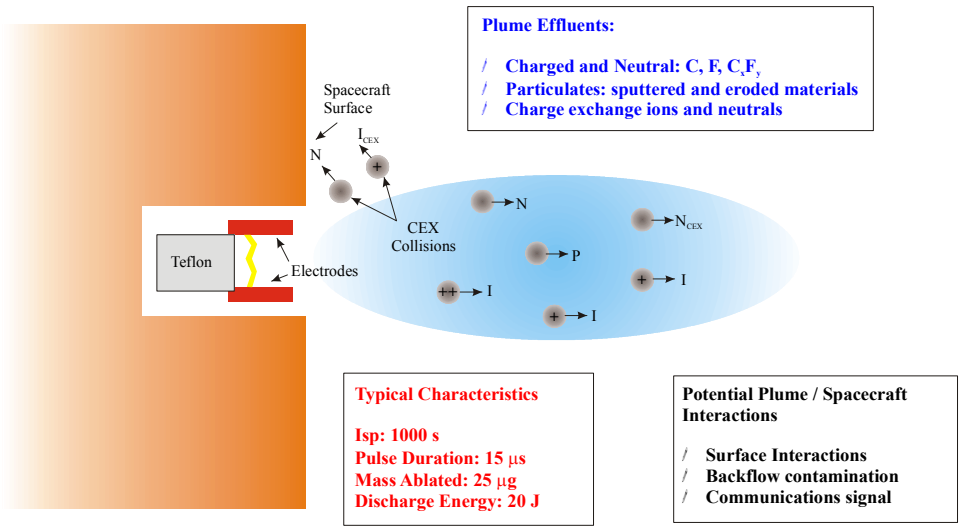

Figure 1.2 Composition of a PPT plume (from Gatsonis et al. 2001).

Since PPTs don't have the benefit of a long and proven flight history there exists a need for experimental as well as computational modeling of PPT plumes. Knowledge of the components of the plume is essential in understanding its possible effects on spacecraft and can be better understood through experimentation. Knowledge from these experimental investigations can be used to build complex computer simulations of the exhaust plume flows. These simulations will aid in the process of understanding the physics involved in PPTs. These endeavors will give spacecraft designers a better understanding of the induced environment from PPTs and will allow the integration of PPTs into spacecraft so that they can maximize the benefits PPTs can offer, while minimizing the potential impact they may have on the spacecraft and its payload.

Worcester Polytechnic Institute's (WPI) Computational Gas and Plasma Dynamics Laboratory (CGPL) has undertaken research both computationally and experimentally into PPTs and Micro-PPTs. The objectives of the PPT program are to investigate experimentally the PPT plume in order to develop an advanced validated

predictive ability for the exhaust plumes of a PPT and their induced environments about spacecraft, (see review by Gatsonis et al. 2001). This thesis presents the development and application of double and triple Langmuir probes for use in the PPT plume environment. These are plasma diagnostics that allow for the measurement of electron temperature and density of the PPT plume, two important parameters in characterizing a plasma. Experimental work was carried out at the NASA Glenn Research Center vacuum facilities. By obtaining a better understanding of the plume composition and acceleration mechanisms of the plasma species, this PPT program can assist in the design and optimization of PPTs.

1.1 Review of Experimental Investigations

The first experimental investigation into a PPT was performed by Vondra et al. [1970] using the LES-6 PPT. They determined that during each 5 kA current pulse, 1.85-J discharge, approximately 10^{-8} kg of Teflon® was ablated or $6x10^{16}$ molecules of $(C_2F_4)_n$. They found an exhaust velocity of 3000 m/s, an I_{sp} of 300 s, and an impulse bit of 31.2 μN-s. The ion velocity was determined to be approximately 40,000 m/s with Faraday cup measurements and they surmised that the gas was only partially ionized. Using a single Langmuir probe they determined a typical electron temperature 2.5 cm from the Teflon® surface to be approximately 20 eV 4 μs after the start of the discharge. Evidence of C^{++} and F^{++} were seen in spectral lines. Using a K-band microwave

interferometer, estimates of electron density were found to be on the order of 10^{18} m^{-3} , Vondra et al. [1970].

Thomassen and Vondra [1972] continued the investigation into the LES-6 PPT using a scanning spectrometer that identified C, F, C^{+}, F^{+}, C^{++}, F^{++}, C^{+++}, F^{+++}, as well as some weak traces of iron from sputtering. They found that most of the neutrals were created after the discharge and that initially the discharge was highly ionized. They conclude that more than 90% of the exhaust was made up of neutral atoms and molecules.

Guman and Begun [1977] determined that the PPT plume was confined with ±40º of the thruster centerline. A double Langmuir probe was used to determine a peak ion density of $3.5x10^{20}$ m^{-3} at a distance of 0.7 m from the exit plane. The maximum electron temperature was found to be 3.7 eV. Their results showed a drop off in both electron temperature and ion density as they moved further off-axis from the centerline. Of interest in this study is that an in-situ cleaning method was used for their Langmuir probes, which was determined to be necessary after approximately 20 pulses of the thruster. Simulated solar cells were placed within the plume in an attempt to determine any detrimental effects. They did not find the PPT plume to be highly contaminating..

Hirata and Murakami [1984], investigated a PPT used on the Japanese ETS-IV mission. Using a mass spectrometer, they determined the presence of C, F, CF, CF_2, and CF_3 in the plume. The velocity of the ions in the plume was also determined to be 34,000 m/s.

Markusic and Spores [1997] investigated the spectroscopic emission of a rectangular-geometry PPT. Through the observation of optical emissions from the PPT,

they were able to determine some of the plasma parameters. The presence of F, F^+, C^+, C^{++}, and C_2 were observed. They did not notice the presence of C and CF as observed by Hirata and Murakami [1984]. However, this is likely due to not examining the UV and IR regions where they believed these species would have occurred. They were able to determine a time-averaged electron temperature of 1.4 ± 0.2 eV.

Antropov et al. [1997] used laser interferometers and Langmuir probes to measure plasma parameters of a Russian PPT operating at energy levels of 80-100 J. It was determined that the plasma moved in two parts, a fast portion that traveled at approximately 30-40 km/s and slower portion moving at 10-12 km/s. The electron temperature was in the range of 1.8-2.6 eV. Maximum electron densities were on the order of 10^{20} m^{-3} within 15 cm of the propellant surface.

Spanjers et al. [1998] studied the inefficiencies of the PPT propellant usage. Exhaust deposits were collected and examined with a scanning electron microscope and with energy dispersive X-ray analysis. They showed that Teflon® particulates were being ejected during the discharge. The particulate emissions consumed 40 ± 3% of the total propellant mass, but only contributed less than 1% to the total thrust.

In a separate investigation Spanjers et al. [1998] examined the correlation between PPT efficiency and propellant temperature. It was determined that decreasing the propellant temperature increases the propellant efficiency, thruster efficiency, and specific impulse.

Burton and Bushman [1998] used quadruple Langmuir probes to characterize the plume of a coaxial geometry PPT operating at an energy level of 9 J. It was determined that the plume was symmetric and had a peak electron density of 2.0 ± 1.0 x 10^{20} m^{-3}.

The electron temperature was determined to be approximately 2.0 ± 0.3 eV. The ion Mach number was found to be 3.0 ± 0.5. An ion velocity of 34 km/s was found by measuring the arrival time of the peak electron density. A survey of the plume using magnetic probes showed the plume to be asymmetric. This was attributed to a radial electromagnetic thrust component that was believed to be only 4% of the overall thrust.

The EO-1 PPT was studied by Arrington and Haag [1999] using off axis thrust stand measurements. The determined that there existed a significant off-axis thrust component towards the anode electrode with the plume canted towards the cathode electrode. Arrington et al. [2000] subsequently confirmed some of their previous findings on the EO-1 PPT. An array of quartz witness plates was used to collect plume constituents for analysis. Results showed the plume was canted towards the cathode. The transmittance losses of the films deposited on these plates was investigated but showed a negligible loss of transmittance from the deposition.

Studies of the LES 8/9 PPT were performed by Myers, et al. [1996] and by Gatsonis, et al. [2001]. The studies involved contamination assessment using quartz crystals, measurements of ion current density using planar Langmuir probes, and ion velocity measurements using a single Langmuir probe. The quartz crystals revealed that measurable changes in transmittance were confined to 30 degrees from the centerline of the thruster. Ion density 24 cm downstream from the thruster was found to be 6×10^{18} m^{-3}. Two distinct ion velocity peaks were seen, one traveling at 60 km/s and a second later peak traveling with a velocity of 30 km/s.

A comprehensive survey of the plume of a laboratory PPT similar to the EO-1 PPT was performed by Eckman, et al. [2001]. Triple Langmuir probes were used to

determine electron temperature and density at radial distances within 20 cm of the propellant surface and at polar angles less than 45 degrees from the centerline. Large variations of the plume properties were seen in the plane perpendicular to the thruster electrodes, while only small variations were seen in the plane parallel to the electrodes. The average maximum electron temperature ranged from 2-4 eV for all discharge energy levels considered. The average maximum electron density is 1.6×10^{20} m^{-3}, 1.6×10^{21} m^{-3}, and 1.8×10^{21} m^{-3} for the 5-J, 20-J, and 40-J discharge, respectively. The time-average electron density increases with increasing discharge energy and are in the range between 10^{19} to 2×10^{20} m^{-3} for a 5-J discharge, 6×10^{20} to 10^{21} m^{-3} for a 20-J discharge, and 2×10^{20} to 1.4×10^{21} m^{-3} for a 40-J discharge.

1.2 Objectives and Methodology

The purpose of this thesis is to provide an expanded insight into the plume of a PPT with the aid of plasma diagnostic techniques. This will primarily be accomplished through the use of triple Langmuir probes, a plasma diagnostic technique for instantaneously determining the electron temperature and number density of a plasma. The applicability of this method to the plume of a PPT will be examined through theory as well as by comparison to data taken with a double Langmuir probe.

This work builds upon and considerably refines WPI's previous PPT plume investigation [Eckman, 1999] in several ways. First, the measurements were conducted in a large vacuum facility in order to better accommodate the expansion of the plume and to reduce facility effects. Second, measurements covered the entire plume from the

thruster centerline out to the backflow regions in both directions. Third, the triple Langmuir probes were operated in what shall be referred to as the current-mode method. This was the first modern application of triple probes in this manner to any electric propulsion device. Fourth, the ion current collection theory uses the Peterson and Talbot [Peterson and Talbot, 1970] fits to Laframboise's theory [Laframboise, 1966] that accounts for effects of the sheath expansion on current collection and the Bohm current collection theory for points that fall outside of Laframboise's theory. Fifth, formal uncertainty analysis was developed based upon the full set of non-linear equations describing the triple Langmuir probe operation. The detailed evolution of this diagnostic can be found in Byrne, et al. [2000, 2001, and 2002].

Objectives of this thesis are:

- Design and develop an experimental setup and procedures for plume measurements in a large vacuum facility.
    - Test stand was designed and built to mount PPT along centerline of vacuum facility and allow for repositioning PPT in an alternate alignment.
    - Probe motion system was designed and built to remotely position the probes within the PPT exhaust plume on two axes.
    - Procedures were developed for in-situ cleaning of probes (glow cleaning) in this new facility.
- Operate laboratory parallel plate PPT for all experiments at energy levels of 5, 20, and 40 J.

- Obtain electron temperature and density measurements using double Langmuir probes.
- Obtain electron temperature and density measurements using triple Langmuir probes operating in the current-mode.
    - Current collection theory of Laframboise was applied to current-mode triple Langmuir probes.
- Take measurements in the far off-axis regions and into backflow area.
- Perform error analysis following the method outlined by Gatsonis, et al. [2002].
- Apply necessary numerical algorithms to solve the complex systems of non-linear equations describing the current-mode triple Langmuir probe.

The experimental work of this thesis ties directly into the concurrent computational models being developed by WPI in two ways. First the experimental data will be used to test the validity of these models. Virtual probes can be placed into the model to determine what the model predicts for plasma properties at various locations. Values from these virtual probes can then be compared to actual experimental data collected at these same locations. Second the experimental data obtained at the exit plane of the thruster can also used as an inputs into the model. Accurate initial and boundary conditions are necessary to get the best results at downstream locations.

This thesis is organized in the following way. Chapter 2 provides an overview of the experiment and the plasma diagnostics used. The theory behind the diagnostics is described in some detail here. The experimental procedures are also outlined. Chapter 3

includes data reduction techniques used and a presentation of the results. The final chapter presents some conclusions reached based upon the results of Chapter 3.

Chapter 2 Experimental Setup, Diagnostics, and Procedures

2.1 Thruster, Facility, and Experimental Apparatus

As with most EP devices, the PPT can only be effectively operated in space or in a facility designed to simulate space vacuum conditions. The resources required to maintain and operate a large vacuum facility such as high pumping rates, are beyond the means of most universities and organizations. As such, this experiment was conducted entirely on site at NASA Glenn Research Center in Cleveland, Ohio.

2.1.1 Pulsed Plasma Thruster

The thruster used in this experiment is a laboratory model designed by NASA GRC similar to the EO-1 thruster to be used for component life testing and plume studies. It has a parallel plate electrode arrangement with a rectangular geometry housing as can be seen in Figure 2.1.

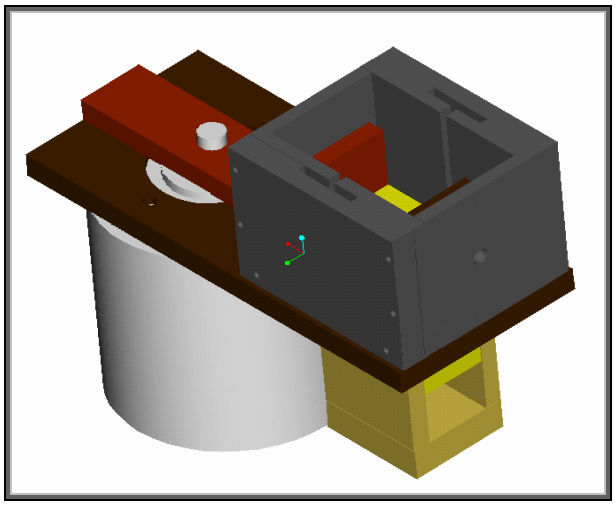

Figure 2.1 Schematic of the NASA GRC laboratory PPT.

The rectangular electrodes have a length and width of 2.54 cm and are made from copper. A block of Teflon® is contained within a fuel bar housing made of Torlon® located directly below the electrodes. The fuel bar is fed up between the electrodes by a spring. A small notch in the anode electrode is used as a fuel retaining shoulder to hold the fuel bar in place. A rectangular Torlon® housing surrounds the electrodes and acts as a sputter guard and a baffle to confine and collimate the exhaust to an extent.

The cathode has a Unison aircraft engine sparkplug imbedded within it which is ignited by a Unison igniter box. Low voltage lines are fed to the igniter box to supply it with power. The output of the igniter box is a high voltage pulse that creates an electric discharge across the spark plug when triggered. A Hyperion 18 V – 10 A power supply was used to power the igniter box. The igniter box is placed within the vacuum facility in close proximity to the PPT in order to minimize the length of the high voltage leads. A push button switch in series with the low voltage lines is used to trigger the igniter box and initiate a PPT pulse.

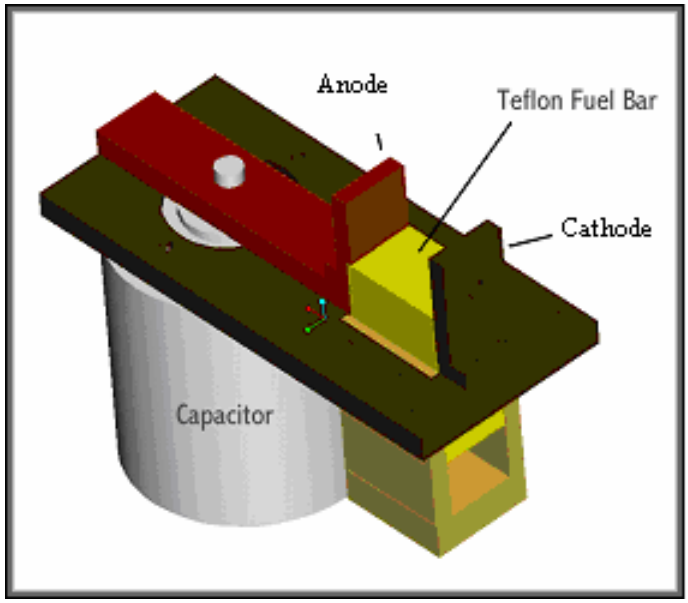

Figure 2.2 Schematic of the GRC laboratory PPT without sputter guard.

The PPT electrodes are biased with a Maxwell 33 μF, 2000 V oil filled capacitor. The capacitor is integrated into the PPT design and can be seen as the gray cylinder in Figure 2.2. A Rogowski coil is bonded into place between the anode and cathode posts of the capacitor using Torr Seal® and is used to measure the current flowing out of the capacitor. A Glassman 3.0 kV, 200 mA high voltage power supply is used to charge the capacitor. The PPT could be operated at a range of discharge energy levels from 5-J to 60-J. The charge voltage was varied to achieve the desired discharge energy of the PPT.

The thruster is similar in size and performance to the EO-1 PPT. The operational characteristics are shown in Table 2.1.

Table 2.1 Operational characteristics of the GRC laboratory PPT

Discharge Energy (J)	Impulse Bit (μN-s)	Mass Loss/Pulse (μg/pulse)	Specific Impulse (s)
5.3	36	-	-
20.5	256	26.6	982
44.0	684	51.3	1360

2.1.2 Vacuum Facility

The vacuum facility CW-19 (Figure 2.3) used in these experiments is part of NASA GRC's electric propulsion laboratory. This cylindrical tank has a diameter of 2.13 m and a length of 3.05 m with a volume of approximately 6.22 m^3. This volume was estimated to be large enough to allow the PPT plume to expand without obstruction and minimize effects from the plume interacting with the tank walls.

The facility is pumped by two 0.89 m diameter oil diffusion pumps backed by a mechanical roughing pump. This system was able to achieve an estimated pumping speed of 12,500 L/s on nitrogen. This facility had the ability to isolate the main chamber via large gate valves from the oil diffusion pumps. This allows for faster turnaround times and provides the ability to clean the probes in-situ through a glow cleaning method without shutting the facility down.

The system was roughed down using the mechanical roughing pump to a pressure of $5x10^{-2}$ Torr at which point the gate valves to the oil diffusion pumps were opened. The diffusion pumps operate by heating high molecular weight oil into a vapor that rises up through the diffusion pump and is sprayed, thereby trapping air molecules within the oil vapor. The oil vapor is then collected on a water cooled condenser. The condensed oil with the trapped air molecules will then travel down to the bottom of the diffusion pump

were the air molecules can be mechanically pumped out by the Stokes blower. The facility was able to maintain a pressure of $5x10^{-7}$ – $2x10^{-6}$ Torr during the operation of the thruster.

Figure 2.3 Vacuum facility and instrumentation racks.

Access to the facility was achieved through two rollaway end caps, allowing for easy installation of hardware. There were two mounting points for hardware both located over the oil diffusion pumps at either end of the tank. Instrumentation was wired through feed through flanges on the side of the tank. One flange contained four electrically-isolated BNC type connectors that were used for passing probe and Rogowski coil signal lines through. The power lines were fed through a flange that contained a

seven pin lug type connector. The motion control system lines were fed through a Douglas Engineering 21 pin connector flange.

This experiment was the first use of this facility for EP research. As a result, this project entailed a great deal of facility modification and buildup. Operational procedures also had to be modified for some aspects of the experiment. This was also the first use of TLPs on a PPT in such a large facility.

2.1.3 Test Stand and Probe Motion System

The ability to remotely position the probes through a range of positions in the plume was essential to this experiment. To this end, a probe motion system was designed and built to accomplish both translational and rotational motions. A schematic of the whole PPT and probe motion system with the PPT shown in the parallel plane configuration can be seen in Figure 2.4.

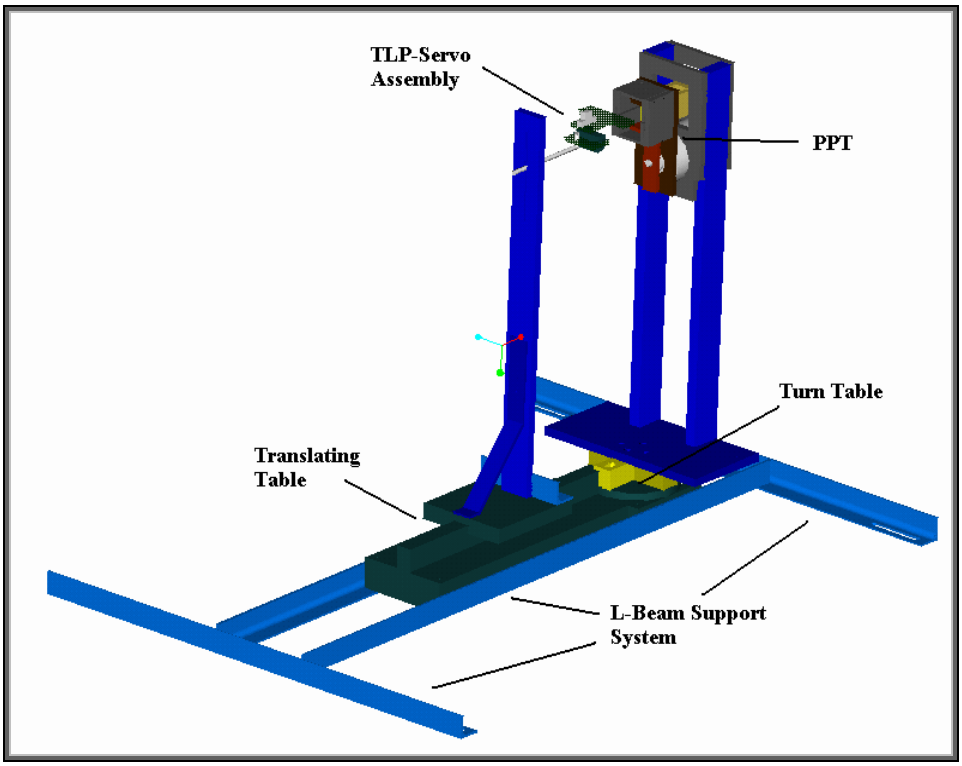

Figure 2.4 Schematic of entire laboratory PPT and probe motion system.

The probes were positioned through a range of downstream locations that would extend from within the thruster to a distance of 20 cm downstream. The origin for the coordinate system is located at the center of the face of the Teflon® propellant with the z-axis extending downstream. Downstream measurements are needed at angular locations off the centerline of the PPT that could be extended to the backflow region (±90º from PPT centerline). The 90º position would be the thruster centerline and 0º and 180º would be the backflow region. Measurements were desired on the plane perpendicular to the electrodes and the plane parallel to the electrodes. The probe axis would also need to be rotated with respect to the PPT axis in order to determine the plume flow vector.

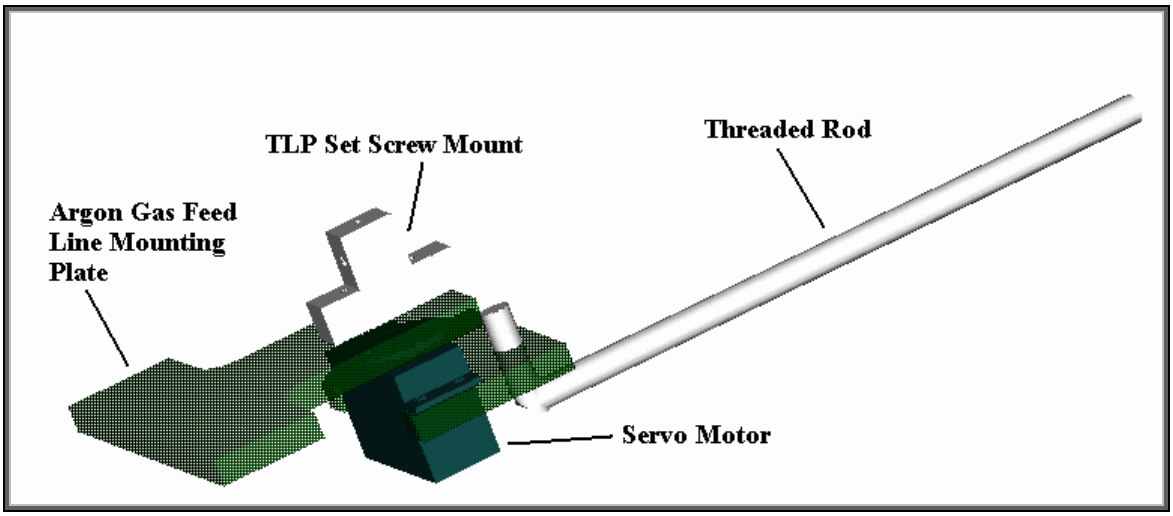

Figure 2.5 Probe mount showing glow cleaning electrode and servo motor for probe axis rotation.

To rotate the probe axis, the probes were mounted onto a small servo-motor controlled mount. A mounting plate was designed to hold the probes and was attached to the servo-motor (Figure 2.5). The servo-motor was capable of rotating the probes a full 180º. The servo-motor allowed for control from outside of the tank using a simple feedback loop circuit. A 10-turn potentiometer controlled the rotation of the mount. The mount's position was read out on a LCD digital display unit as a voltage measurement that could be converted to an angular position. An electronic diagram of the circuit is shown in Figure 2.6. The control circuit was attached to the servo-motor by five wires that were passed through one of the electronics feed through flanges on the facility. The probe servo-motor system failed shortly after testing began. The servo-motor used to rotate the probe itself was from the radio controlled aircraft industry. It was chosen for its low cost, small size and mass. However it was not designed for vacuum use. The small DC motor inside would severely overheat and quickly become useless. The supply of these motors was limited to two and was quickly exhausted. So no useful data was

acquired as to the plasma flow vector. For the remainder of the testing the probe was fixed in a position pointing at the center of the Teflon® surface.

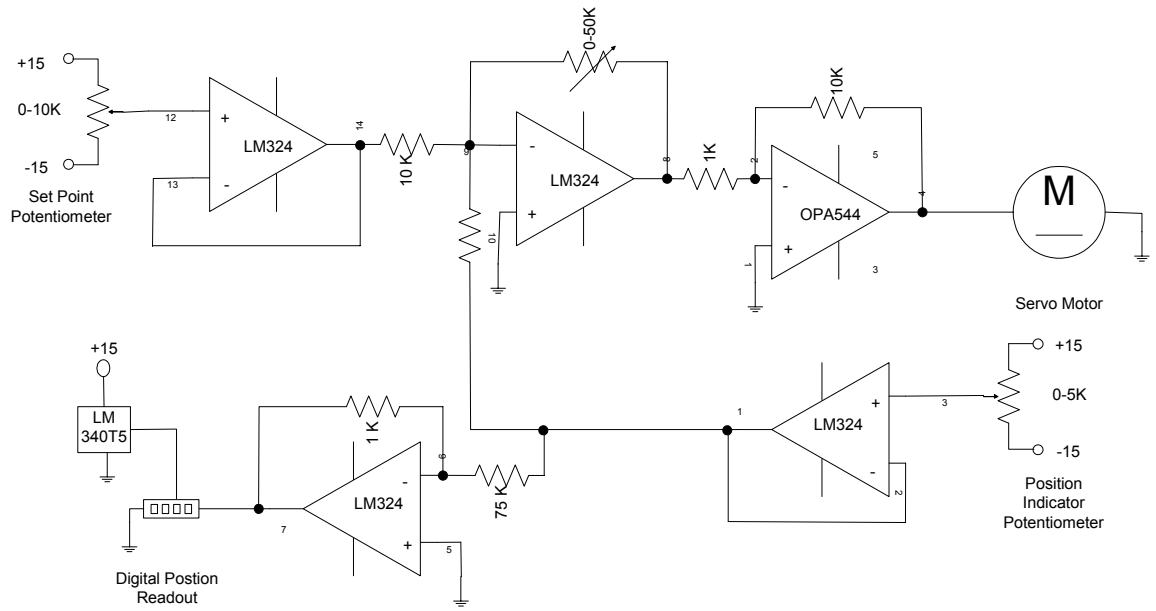

Figure 2.6 Servo control circuit diagram.

The servo assembly also contained a strip of aluminum sheet metal that served as a cleaning electrode. This cleaning electrode was located in close proximity to the exposed probe leads and was used during the glow-cleaning procedure. The cleaning electrode was not active at anytime other than during glow-cleaning. A neoprene® tube was attached near this cleaning electrode. This ran down to a flexible stainless steel braided Argon gas line that was mounted further back on the probe arm. This Argon line was also used during the glow-cleaning process and remained off at all other times. Both the Argon gas line and the cleaning electrode were positioned slightly downstream of the probes as not to interfere with their operation as the plasma wave passed.

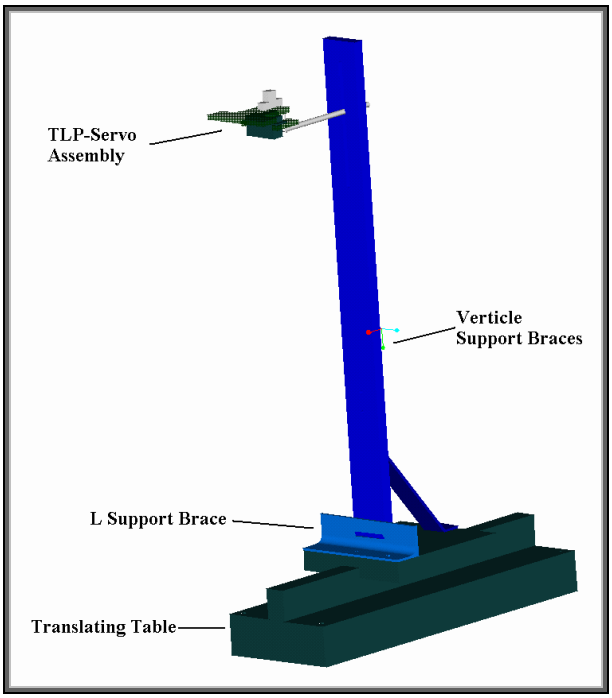

Figure 2.7 Probe motion system.

The entire probe rotation system was attached to an adjustable vertical arm shown in Figure 2.7. This allowed flexibility in aligning the probe with the PPT. The probe could be manually aligned in three axes. This probe arm was attached to a linear translation table manufactured by Daedal, Inc that allowed a linear range of approximately 25 cm and was controlled externally by a computer system.

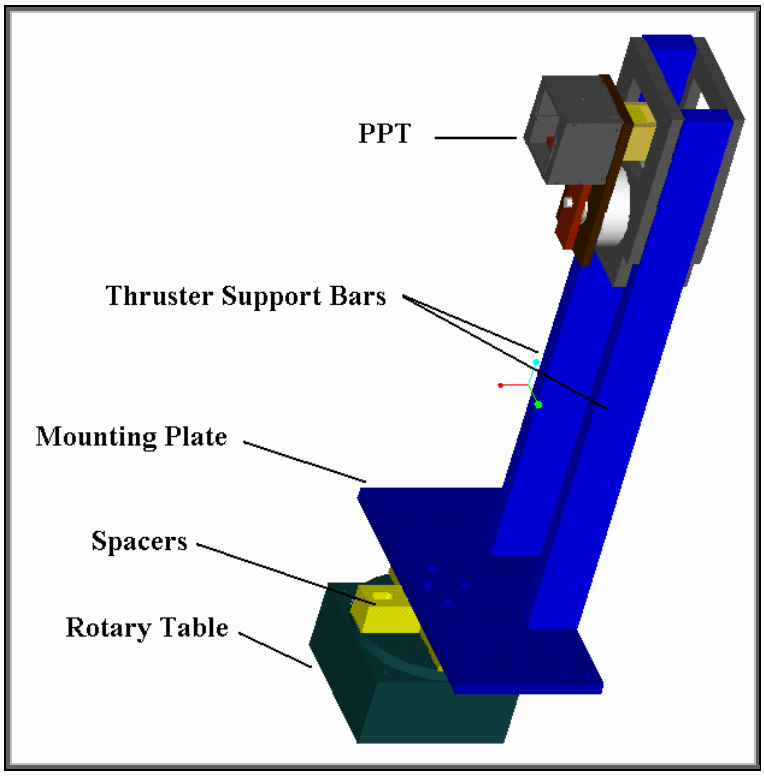

Figure 2.8 PPT mounting system.

To achieve the off-centerline measurements the entire PPT itself was rotated as shown in Figure 2.8. The PPT was mounted upon a turntable manufactured by Daedal, Inc capable of rotating the PPT through a full 180º. The turntable was also controlled externally by the same computer system. The mounting system allowed the PPT to be mounted in two separate positions to achieve measurements in both planes of the PPT.

To allow the PPT plume to expand with minimal obstruction the large volume of the vacuum facility needed to be utilized. To accomplish this, the PPT stand and probe motion system were designed to locate the PPT at one end of the vacuum facility. The PPT was positioned in such a way that its exhaust centerline was aligned with the centerline of the vacuum facility and would travel lengthwise down the tank from one end to the other. In both the perpendicular plane and parallel plane configurations, the

center of the propellant face was aligned with the centerline of the vacuum facility. A picture of the entire system installed into the vacuum facility can be seen in Figure 2.9. The PPT is in the parallel plane configuration rotated to the $\theta_{\parallel} = 90^{\circ}$ position, so that only the backside of the PPT is visible from this angle. The spark plug igniter box can also be seen as the metallic box in the lower left corner of the picture sitting on the support rails.

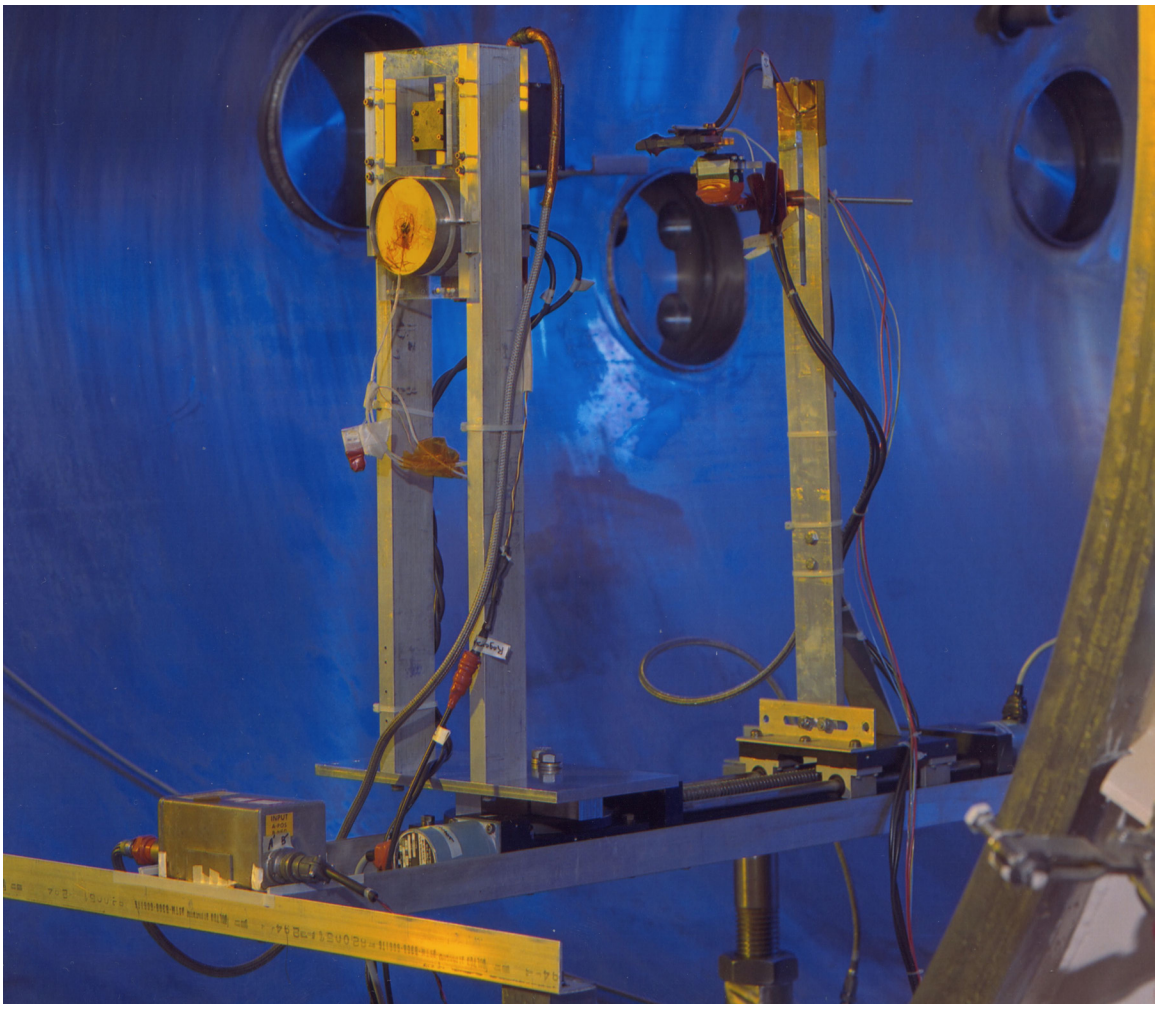

Figure 2.9 PPT and probe motion system installed in vacuum facility.

Design and construction of the PPT and probe motion system was aided by a team of WPI undergraduate students as part of their Major Qualifying Project (see Krumanaker, et al., 1999).

2.2 Triple and Double Langmuir Probe

To gain a better insight into the operation of a PPT and its interaction with its environment it is important to characterize its exhaust plume. There exists a broad range of plasma diagnostics available to an experimentalist and this thesis focused on double and triple Langmuir probe techniques. These techniques allow for the evaluation of electron temperature and density of the plasma. In this chapter the theory behind the current-mode triple and double Langmuir probe are outlined.

2.2.1 Triple Langmuir Probe Theory

Triple probe theory is a plasma diagnostic technique for instantaneously measuring electron temperature $T_e(t)$ and electron number density $n_e(t)$. It was first outlined by Chen & Sekiguchi [1965] for use in collisionless, Maxwellian, two-temperature plasmas. Triple Langmuir probes (TLP) do not require a voltage or frequency sweep common to other Langmuir probe methods. This eliminates the time consuming data analysis required in curve-fitting current-voltage characteristics in order to obtain plasma parameters. In addition, this feature makes TLPs ideal for time varying plasmas and plasmas that have fast transients such as found in the plume of a PPT.

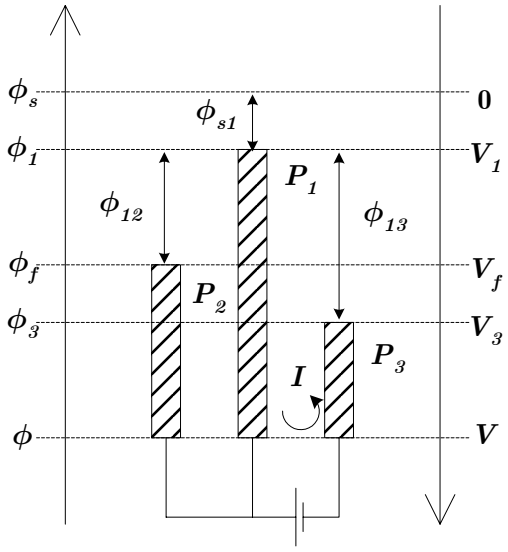

Figure 2.10 Diagram of electric potential for a direct-display triple Langmuir probe.

A symmetric triple Langmuir probe, similar to the ones used in this experiment, consists of three identical probes placed in the plasma. In the traditional mode of operation, referred to as direct-display or voltage-mode, one of the probes, indicated as probe-2 in Figure 2.10, is allowed to electrically float in the plasma and a fixed bias voltage ϕ_{13} is applied between the positive and negative probe with respect to the floating potential probe. The resulting voltage difference $\phi_{12}(t)$ and collected current $I(t)$, allow for the evaluation of $T_e(t)$ and $n_e(t)$. Triple probes have been used successfully in the past in the steady plumes of magnetoplasmadynamic (MPD) thrusters (Tilley 1990, Gallimore 1990), arcjets (Bufton et al., 1995), Hall-Effect Thrusters (Fife 1998), and the unsteady plume of a PPT (Eckman 2001).

However, the PPT differs from many of these other thrusters in that it is not a steady state device and emits a considerable amount of radiated electromagnetic noise

during the spark initiation and the discharge of its main capacitor. The voltage measurement needed to obtain $\phi_{12}(t)$ is a high impedance measurement that is easily susceptible to noise entering the system. Chen and Seckiguchi (1965 and 1971) also outlined a technique that does not rely on a voltage measurement but rather on current measurements. This method will be referred to as the current-mode TLP theory, which was used in this experiment and is illustrated in Figure 2.11. A fixed voltage ϕ_{12} is applied between probe-1 and probe-2 while another fixed voltage ϕ_{13} is applied between probe-1 and probe-3. The collected currents $I_1(t)$, $I_2(t)$, and $I_3(t)$ allow for the evaluation of $T_e(t)$ and $n_e(t)$ as outlined below.

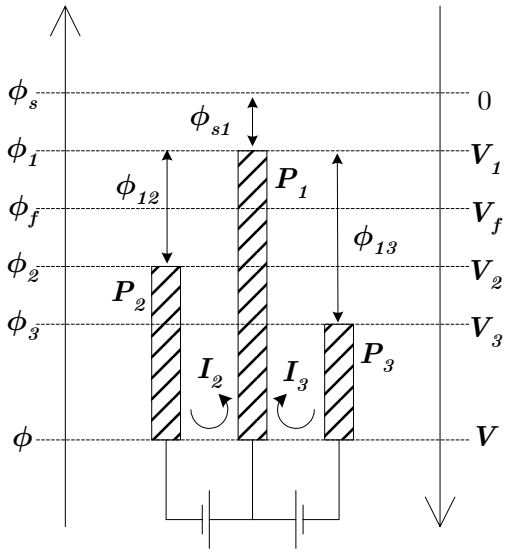

Figure 2.11 Potential diagram for the Current-Based triple Langmuir probe Diagram.

In order to develop the theory of current-based triple Langmuir probe operation we assume that the probes are inserted in a two-temperature flowing plasma whose ion and electron distribution function is a drifting Maxwellian

$$f_{e(i)}(\mathbf{r},\mathbf{v},t) = n_{e(i)}(\mathbf{r},t)\left(\frac{m_{e(i)}}{2\pi k T_{e(i)}}\right)^{3/2} \cdot \exp\left[-\frac{m_{e(i)}(\mathbf{v}_{e(i)} - \mathbf{U}_{e(i)})^2}{2kT_{e(i)}}\right] \tag{2.1}$$

where, $m_{e(i)}$ is the mass, $\mathbf{v}_{e(i)}$ is the particle velocity, $n_{e(i)}(\mathbf{r},t)$ is the number density, $\mathbf{U}_{e(i)}(\mathbf{r},t) = \langle \mathbf{v}_{e(i)} \rangle$ is the average (or drift) species velocity (brackets indicate average over the species distribution function), and $T_{e(i)}$ is the species temperature. We further assume that all three probes are aligned with the plasma flow.

The current collection theory requires that the probes are operating in the collisionless plasma regime,

$$r_p \ll \lambda_{ei}, \lambda_{ee}, \lambda_{en}, \lambda_{ii}, \lambda_{in}\,, \tag{2.2}$$

that the sheath be collisionless,

$$d_S \ll \lambda_{ei}, \lambda_{ee}, \lambda_{en}, \lambda_{ii}, \lambda_{in}\,, \tag{2.3}$$

and that there are no sheath-interactions between the probes,

$$d_S < s\,. \tag{2.4}$$

For a probe electrode at some potential less than the space potential $\left(\phi_p \le \phi_s\right)$ as shown in Figure 2.11 the total probe current is

$$I_p = I_{ep} - I_{ip}\,. \tag{2.5}$$

In writing the above equation, we assume that the electron current to a probe (retarded current) is positive and the ion current (accelerated current) to a probe negative. A probe therefore collects electrons if $I_p > 0$ and ions if $I_p < 0$.

For a probe $\left(\phi_p \le \phi_s\right)$ the electrons are the repelled species and the electron current is given by

$$I_e = A_p J_{eo} \exp\left(-\frac{e\left(\phi_s - \phi_p\right)}{kT_e}\right) = A_p J_{eo} \exp\left(-\frac{e\phi_{sp}}{kT_e}\right) \tag{2.6}$$

where the random electron current to the probe is

$$J_{e0} = en_e \left(kT_e/2\pi m_e\right)^{1/2}. \tag{2.7}$$

The ion current to a cylindrical probe aligned with the flow operating in the collisionless regime depends on the Debye ratio r_p/λ_D, the speed ratio, the temperature ratio T_i/Z_iT_e and the non-dimensional potential

$$\chi_p = (\phi_p - \phi_s)\Big/\left(kT_e/Ze\right) \tag{2.8}$$

The Debye length, assuming a quasi-neutral plasma, $n_i \cong n_e$, is

$$\lambda_D = \sqrt{\varepsilon_o kT_e/e^2 n_i}. \tag{2.9}$$

For $5 \le r_p/\lambda_D \le 100$, $\chi_p > 3$ and $T_i/Z_iT_e \le 1$ Petersen and Talbot (1970) give the ion current to a probe aligned with the flow by an algebraic fit to Labramboise (1966) data as

$$I_i = A_p J_{i0} \left(\beta + \left|\chi_p\right|\right)^{\alpha} \tag{2.10}$$

where the random ion current to the probe is

$$J_{i0} = en_i \left(kT_e/2\pi m_i\right)^{1/2}. \tag{2.11}$$

The parameters α and β are given as

$$\alpha = \frac{2.9}{\ln\left(r_p/\lambda_D\right)+2.3} + 0.07\cdot\left(\frac{T_i}{Z_i T_e}\right)^{0.75} - 0.34 \tag{2.12}$$

$$\beta = 1.5 + \left(T_i/Z_i T_e\right)\cdot\left\{0.85 + 0.135\left[\ln\left(r_p/\lambda_D\right)\right]^3\right\}. \tag{2.13}$$

Applying equations (2.6) and (2.10) to equation (2.5) for all three probes and assuming that $A_1 = A_2 = A_3 \equiv A$ we obtain the following system:

$$\begin{aligned}
I_1 &= A_p J_{eo}\exp\left(-\frac{e\phi_{s1}}{kT_e}\right) - A_p J_{i0}\left(\beta + \frac{e\phi_{s1}}{kT_e}\right)^{\alpha} \\
I_2 &= A_p J_{eo}\exp\left(-\frac{e\left(\phi_{s1}+\phi_{12}\right)}{kT_e}\right) - A_p J_{i0}\left(\beta + \frac{e\left(\phi_{s1}+\phi_{12}\right)}{kT_e}\right)^{\alpha} \\
I_3 &= A_p J_{eo}\exp\left(-\frac{e\left(\phi_{s1}+\phi_{13}\right)}{kT_e}\right) - A_p J_{i0}\left(\beta + \frac{e\left(\phi_{s1}+\phi_{13}\right)}{kT_e}\right)^{\alpha}
\end{aligned} \tag{2.14}$$

The solution to the system of non-linear algebraic equations (2.14) provides n_e, T_e, and ϕ_{s1}.

For $r_p/\lambda_D > 100$, outside of the Peterson and Talbot (1970) range we use the thin-sheath current collection model that assumes the ion current to a probe is independent of the bias voltage, i.e.,

$$I_i\left(\phi_s - \phi_1\right) = I_i\left(\phi_s - \phi_2\right) = I_i\left(\phi_s - \phi_3\right) \equiv I_i\,. \tag{2.15}$$

The ion current to the probe can then be approximated as the ion current to the sheath that is given by the Bohm expression:

$$I_i = A_p e n_e \sqrt{kT_e/m_i}\,\exp^{-1/2}. \tag{2.16}$$

The above expression assumes that there is a single ion species in the plasma and that $T_e \gg T_i$. The full system using the thin-sheath equation is as follows:

$$
\begin{aligned}
I_1 &= A_p J_{eo} \exp\left(-\frac{e\phi_{s1}}{kT_e}\right) - A_p e n_e \sqrt{kT_e/m_i}\, \exp^{-1/2} \\
I_2 &= A_p J_{eo} \exp\left(-\frac{e\left(\phi_{s1}+\phi_{12}\right)}{kT_e}\right) - A_p e n_e \sqrt{kT_e/m_i}\, \exp^{-1/2} \\
I_3 &= A_p J_{eo} \exp\left(-\frac{e\left(\phi_{s1}+\phi_{13}\right)}{kT_e}\right) - A_p e n_e \sqrt{kT_e/m_i}\, \exp^{-1/2}
\end{aligned}
\tag{2.17}
$$

Following Chen and Sekiguchi (1965) the system (2.17) can be manipulated into easily solvable expressions for T_e and n_e.

$$
\frac{I_1 - I_2}{I_1 - I_3} = \frac{1 - \exp\left(-\frac{e}{kT_e}\phi_{12}\right)}{1 - \exp\left(-\frac{e}{kT_e}\phi_{13}\right)} \tag{2.18}
$$

$$
n_e = \frac{\frac{1}{A}\dfrac{I_3 - I_2 \exp\left\{-\frac{e}{kT_e}\left(\phi_{13}-\phi_{12}\right)\right\}}{\exp\left\{-\frac{e}{kT_e}\left(\phi_{13}-\phi_{12}\right)\right\} - 1}}{\exp(-1/2) e\sqrt{kT_e/m_i}} \tag{2.19}
$$

2.2.2 Double Langmuir Probe Theory

In some types of plasma discharges there does not exist an electrode or reference point that is in good contact with the plasma. This reference point is needed when applying a bias voltage to a Langmuir probe. In other situations, the plasma potential may change with time, which will create difficulties in maintaining a constant voltage difference between a probe and the plasma potential. In these situations single Langmuir

probes are not readily applicable and Johnson and Malter (1950) developed a technique that overcomes some limitations of the single probe. It involved the use of two Langmuir probes biased with respect to each other and isolated from ground. This allows the probes to electrically float with regard to the plasma therefore allowing the probes to follow the changes in the plasma potential.

A double probe consists of two electrodes that are inserted into a plasma. The spacing between the probes must be small enough that the properties of the plasma can be taken to be constant over that interval. In the case of a cylindrical double probe, the electrodes are nothing more than two exposed lengths of wire.

Some bias voltage (ϕ_b) is applied between probes 1 and 2.

$$\phi_b = \phi_1 - \phi_2 > 0 \tag{2.20}$$

We shall make ϕ_1 positive with respect to ϕ_2. Since the entire double probe system is not connected to any other electrodes, the system will electrically float. No net current will be drawn by the two probes therefore both probes will be negative with respect to the plasma. A potential distribution is shown in Figure 2.12.

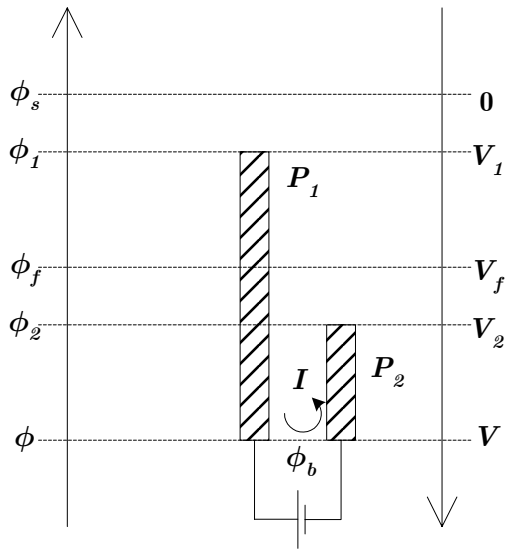

Figure 2.12 Potential diagram for a double Langmuir probe.

A typical probe I-V characteristic is shown in Figure 2.13. The symmetry of this curve is due to the probes having equal areas. At point C in Figure 2.13, $\phi_b = 0$ and no net current is being drawn by either probe, therefore the probes are at the floating potential of the plasma. At point B, ϕ_1 is becoming less negative while ϕ_2 is becoming more negative with respect to the space potential (ϕ_s). This means that there will be more electrons flowing to probe 1 than to probe 2, which will result in a positive current flow between probe 2 and 1, i.e., current is flowing from probe 2 to 1. At point A, ϕ_1 will be just negative of ϕ_s thus allowing it to collect just enough electron current in order to balance the ion current being collected by probe 2. At this point probe 2 is collecting the saturation ion current. When ϕ_b is negative the current will reverse and the characteristic

curve will be symmetric. Due to the areas of the electrodes being equal, the ion saturation currents will be equal for both probes.

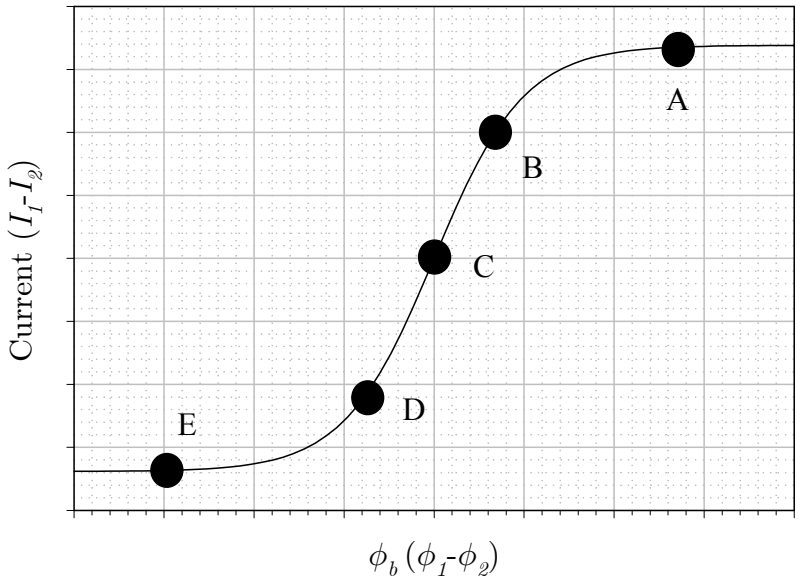

Figure 2.13 Theoretical current-voltage characteristic for probes of equal area.

The double probe has the advantage that the electron current being drawn to either probe will never exceed the ion saturation current which typically is much lower than the electron saturation current. Thus, the disturbance to the plasma by the probes is minimized. However, because of this the electrons either probe is seeing will only be the very energetic ones or the high-energy tail of a Maxwellian distribution. So, the majority of the electrons will not be sampled by this method.

The double probe characteristic seen in experiments may not always be as symmetrical as the theoretical curve. If the current collecting area of the two electrodes are not equal (due to probe contamination perhaps), the magnitude of the saturation

regions (points A and E) may not be the same. In some instances, a potential difference might exist between probe 1 and 2 without a measured current. This would have the effect of shifting the characteristic to either side of the origin. This could be a symptom of the floating or contact potentials not being equal for the two probes. Alternatively, a strong potential gradient may exist in the immediate vicinity of the probes [Schott, 1968].

The condition that the double probe is floating relative to the plasma means that no net current is flowing therefore using equation (2.5) we obtain the following

$$I = I_{i2}^{*} - I_{e2}^{*} = I_{e1}^{*} - I_{i1}^{*} \tag{2.21}$$

The electron saturation current density to a probe in the transition region (ϕ_{probe} near ϕ_{f}) is given by the following equation

$$j_e^{*} = \frac{1}{4} n_e \overline{C_e} e^{\frac{e\phi}{kT_e}} \tag{2.22}$$

The mean speed is given by

$$\overline{C_e} = \sqrt{\frac{8kT_e}{\pi m_e}} \tag{2.23}$$

The electron saturation current density then becomes

$$j_e^{*} = \frac{1}{2} n_e \sqrt{\frac{2kT_e}{\pi m_e}} e^{\frac{e\phi}{kT_e}} \tag{2.24}$$

With this we can obtain the electron saturation current, which is as follows

$$I_e^{*} = A\frac{1}{2} n_e \sqrt{\frac{2kT_e}{\pi m_e}} e^{\frac{e\phi}{kT_e}} = A j_{eo}^{*} e^{\frac{e\phi}{kT_e}} \tag{2.25}$$

where

$$j_{eo} = \frac{1}{2} n \sqrt{\frac{2kT_e}{\pi m}} \tag{2.26}$$

is the random electron current density and A is the current collecting area of the probe. The electron saturation current at probe 1 and 2 is

$$I_{e1}^{*} = A_1 j_{eo}^{*} e^{\frac{e\phi_1}{kT_e}}$$
$$I_{e2}^{*} = A_2 j_{eo}^{*} e^{\frac{e\phi_2}{kT_e}} \tag{2.27}$$

If we substitute this into equation (2.21) using the relationship, $\phi_b = \phi_1 - \phi_2$, after some manipulation we have the following relationship

$$\frac{I + I_{i1}^{*}}{I_{i2}^{*} - I} = \frac{A_1}{A_2} e^{\frac{e\phi_b}{kT_e}} \tag{2.28}$$

This is the general formula for the double probe current as a function of voltage. For a symmetric probe, the areas are equal and the ion saturation currents becomes $I_{i1}^{*} = I_{i2}^{*} \equiv I_i^{*}$. With these simplifications equation (2.28) will become

$$\frac{I + I_i^{*}}{I_i^{*} - I} = e^{\frac{e\phi_b}{kT_e}} \tag{2.29}$$

Further manipulation produces the following.

$$I = I_i^{*} \frac{e^{\frac{e\phi_b}{kT_e}} - 1}{1 + e^{\frac{e\phi_b}{kT_e}}} \bullet \frac{e^{-\frac{e\phi_b}{2kT_e}}}{e^{-\frac{e\phi_b}{2kT_e}}} = I_i^{*} \frac{e^{\frac{e\phi_b}{2kT_e}} - e^{-\frac{e\phi_b}{2kT_e}}}{e^{\frac{e\phi_b}{2kT_e}} + e^{-\frac{e\phi_b}{2kT_e}}} \tag{2.30}$$

Upon further simplification, we obtain the equation of the double probe characteristic for equal area electrodes as follows

$$I = I_i^{*} \tanh\left(\frac{e\phi_b}{2kT_e}\right) \tag{2.31}$$

The value for the ion saturation current in equation (2.31) can be found from experimental data by extrapolating the flat parts of the I-V curve to the y-axis. Using this value for the ion saturation current, the equation for the double probe characteristic can be fitted to experimental data in order to obtain the electron temperature.

Alternatively, another way of determining the electron temperature is through the slope of the I-V curve at the origin $\left(\phi_b = 0\right)$ using the experimental value of ion saturation current. The slope of the I-V curve can be found by taking the derivative of equation (2.31) as follows.

$$\frac{dI}{d\phi} = \frac{I_i^* e}{2kT_e}\operatorname{sech}^2\left(\frac{e\phi_b}{2kT_e}\right) = \frac{I_i^* e}{2kT_e}\frac{4}{e^{\frac{e\phi_b}{kT_e}} + 2 + e^{-\frac{e\phi_b}{kT_e}}} \tag{2.32}$$

The slope at the origin can be calculated to be

$$\left.\frac{dI}{d\phi}\right|_{\phi=0} = \frac{I_i^* e}{kT_e} \tag{2.33}$$

From equation (2.33) the value for T_e can easily be found. Once I_i^* and T_e are known the number density n_e can be found easily from this equation for I_i^*, assuming $n_i = n_e$.

$$I_i^* = \frac{1}{4} A e n_e \overline{C_i} \tag{2.34}$$

Where $\overline{C_i} = \sqrt{\frac{8kT}{\pi m_i}}$ is the mean ion speed. Therefore, a simple rearrangement of equation (2.34) leads to an expression for the number density

$$n_e = \frac{4I_i^*}{Ae\sqrt{\frac{8kT}{\pi m_i}}} \tag{2.35}$$

2.2.3 Probe Construction and Electronics

Two different diagnostic techniques were used during the course of this experiment, double Langmuir probes and triple Langmuir probes. By removing one of the bias voltages on the triple probe it could be used as a double probe.

A cylindrical Langmuir probe is a conducting wire placed into plasma at one end and attached to various electronics at the other. For this experiment, only symmetrical probes were used, in which each of the two or three wires used are of equal exposed length and surface area. The probes in this experiment were made of tungsten wire. Two different sized probes were made, one used 8-mil wire with a radius of $r_p = 1.016 \times 10^{-4}$ m, and the other used 10-mil wire with a radius of $r_p = 1.27 \times 10^{-4}$ m. A piece of four bore alumina tubing was used to hold the wires, as shown in Figure 2.14. This material is able to withstand high temperature and was vacuum compatible. Alumina also is resistant to sputtering and is an insulator. The alumina was 0.102 m long and had an outer diameter of 6.35×10^{-3} m. The holes were spaced 1 mm apart.

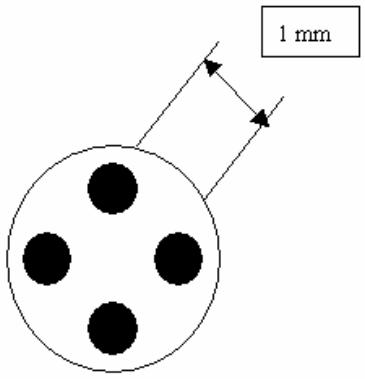

Figure 2.14 End view of probe.

Three equal sized pieces of tungsten wire were cut to a length of 0.203 m. The tungsten wires were fed through three of the four holes with the fourth hole left empty. The wires were cemented into place with Torr Seal® leaving a length of 6 mm exposed on the measuring end. Deutsch® pin style connectors were attached to the other end of the wires to allow connection to a separate cable to carry the signal outside of the tank. This was done to minimize the amount of Tungsten wire used. Each wire was individually covered with silicone shrink-wrap tubing and then bundled together and to the alumina tubing with a larger diameter silicone shrink-wrap tube. This insulated the individual wires from each other and held them in place in the alumina tubing. The triple Langmuir probe design here was derived from Eckman's design [Eckman, 1999].

After several hundred firings of the PPT, it was noticed that the Torr Seal® used to cement the tungsten probes in place to the alumina tubing was deteriorating from the plasma impingement. In addition, carbon soot was building up on it as well causing electrical paths to form that were intermittently shorting the probes. So a subsequent test eliminated the use of the Torr Seal® and just left the tungsten wires held in place by the shrink tubing on the other end.

Three RG-58 coaxial cables were used to carry the signal from the tungsten probes to an acrylic flange with electrically-isolated BNC type connectors on it, (see Figure 2.15). The triple Langmuir probe conductors were attached to the center conductor of the RG-58 cable. The isolated flange was used so as the outer ground ring on the coax cables would be isolated from the tank and could be grounded at the instrumentation rack. This was done in an attempt to minimize any potential EMI noise pickup. The connection between the coax cable and the tungsten probes was insulated

heavily with Kapton® and silicone tape. The cable length inside the tank was 3.65 m. The long length was needed to allow the probe motion system to move unimpeded. The cables were carefully laid out so as not to cross over each other or to come near any other lines inside the tank. They were laid on top of Kapton® sheets to further isolate them from the tank walls.

On the external side of the BNC flange, more RG-58 coax cable was used to connect the probe leads to the instrument rack. The length of this cabling was 3.05 m. The probe leads attached to the outside of the door to the copper Faraday cage. This copper Faraday cage was used to hold the electronics used for the probe measurements. The use of the Faraday cage was an attempt to further reduce any EMI pickup. Within the cage the probe leads were attached to the batteries that supplied the bias voltages.

The bias voltages for the double probe measurements were supplied by alkaline batteries, both D-cell and 9-volt type. The range of bias voltages was $\phi_b \approx \pm 27\,\mathrm{V}$, achieved by various combinations of these batteries.

For the TLP measurements, two bias voltages were needed and they were supplied by the same batteries used for the double probe measurements. The applied $\phi_{13} \simeq 18$ V was supplied by 9-V batteries in series while $\phi_{12} \simeq 3\,\mathrm{V}$ was supplied by D-cell batteries in series. The electrical diagram for this experiment is illustrated in Figure 2.15.

In our experiments the instantaneous current draw reached a peak of approximately 3 A during the 10-15 μs PPT discharge at an energy of 40 J. This instantaneous current draw caused a 24% drop in the bias voltages. The voltage fluctuation was stabilized by the insertion of 40 μf of capacitance in parallel with ϕ_{12} and

ϕ_{13} that reduced the bias voltage deviation to less than 1%, see Byrne, et al (2001). However this capacitance was later determined to adversely affect the measurements by introducing a time shift in the probe-2 current. The final data collection was performed without the use of the capacitors, see Byrne, et al (2002). The small amount of capacitance the RG-58 coax cables possess was believed to have a negligible effect on the measurements. The effect of the bias voltage fluctuations on the reduced data will be accounted for in the uncertainty analysis.

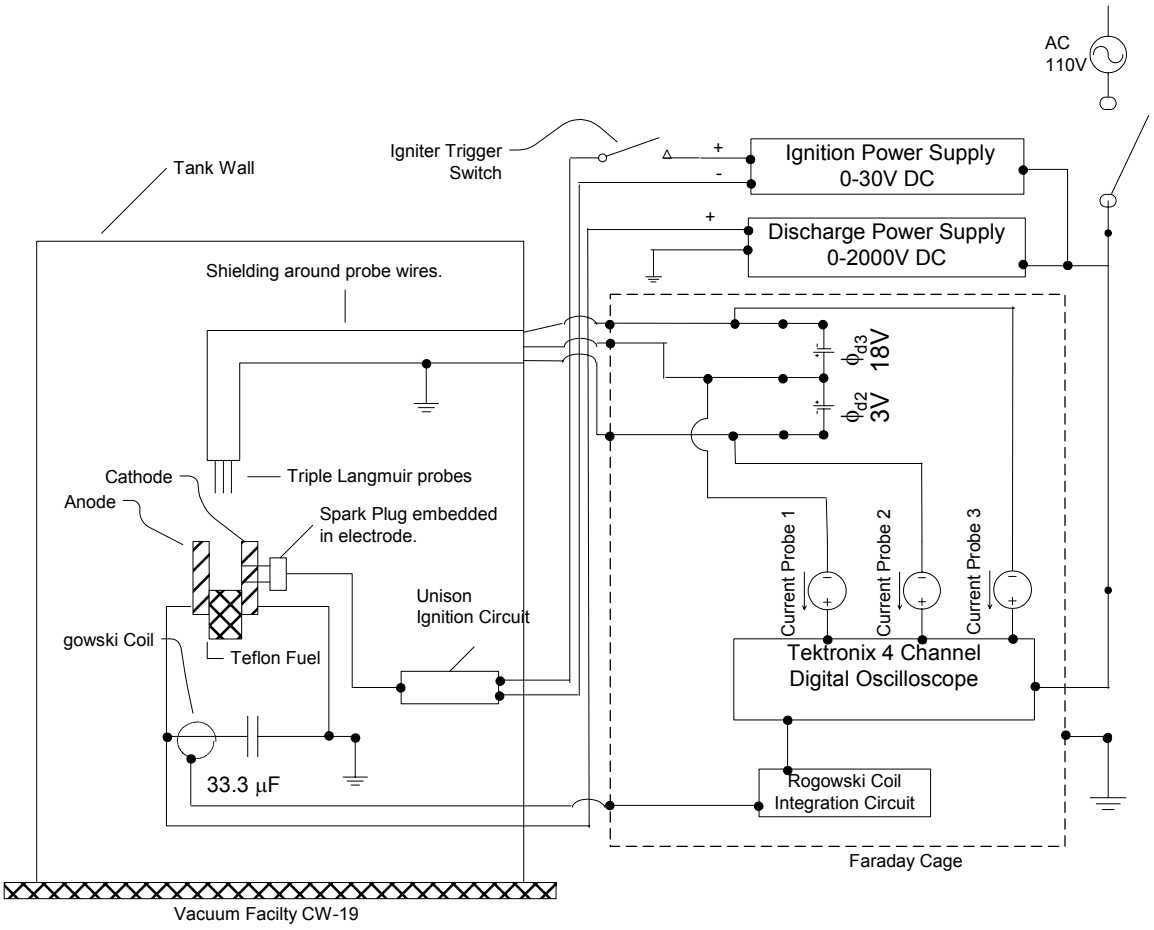

Figure 2.15 Electronics diagram of the triple and double Langmuir probe plume experiments.

An RG-58 coax cable was also used to run the signal for the Rogowski coil embedded in PPT capacitor out of the tank. A 3.65 m length was used inside the tank and connected to the isolated BNC feed-thru flange used by the probe leads. Externally a 3.05 m length ran from the flange to the Faraday cage. From the Faraday cage the Rogowski coil signal was sent to a simple RC integrator circuit box. The value for the resistance was R=5.98 kΩ and the capacitance was C=0.0104 μF.

The measurements were recorded on a Tektronix TDS 754D four channel digital oscilloscope. The oscilloscope had a bandwidth of 500 MHz and a sampling rate of 2 Gs/s. The current flowing through each of the three probes was the measurement of interest. This was measured using three Tektronix TCP202 Hall effect current probes. These probes interfaced with the oscilloscope allowing for display of the current waveforms as a function of time on channels one through three. The integrated Rogowski coil signal was displayed on the fourth channel of the oscilloscope.

2.3 Triple Langmuir Probe Error Analysis

Triple Langmuir probes must operate under collisionless conditions without sheath interactions. Estimates of plasma parameters are obtained assuming that the PPT plume is composed of singly-ionized C^+ and F^+ ions with molar ratio $[C^+]/[F^+] = 0.5$, the electron temperature in the range of 1-10 eV, the electron density is in the range of 10^{18} - 10^{21} m^{-3} and that $0.01 \leq T_i/T_e \leq 1$. Table 2.2 lists all the computed non-dimensional plasma and probe parameters made from these assumptions.

Gatsonis et al. (2002) showed that for the most part the probes operate in the range, $10 \le r_p/\lambda_D \le 100$, within the limits of Laframboise' theory. Also, for a sheath thickness given by equation (2.36), it can be shown that $s/d_s \gg 1$ for all conditions, as shown in Table 2.2. This indicates that no sheath interactions are present.

$$d_s = \left(\sqrt{2}/3\right)\lambda_D \left(2e\phi_{ps}/kT_e\right)^{\frac{3}{4}}. \tag{2.36}$$

For the most part the probes operate in the collisionless regime though at times they may enter the transitional regime. The end-effects parameter is given by equation (2.37).

$$\tau_L = (L_p/\lambda_D)(kT_e/m_i)^{1/2} U_i^{-1}. \tag{2.37}$$

This parameter describes the effect that the end of the probe plays in current collection as compared to the sides of the probe. The end-effect parameter is estimated to be $\tau_L \gg 50$ using a maximum ion speed of $U_i = 30$ km/s for all conditions considered. This range of τ_L ensures that end-effects can be neglected (see Chung, et al. 1975) and that effects of misalignment will not adversely affect these measurements. The triple probe was aligned with the polar angle as measured from the center of the Teflon® surface which may have resulted in probe misalignment with the flow vector. These issues have been discussed by Eckman, et al. (2001) and Gatsonis, et al. (2002).

Table 2.2 Non-dimensional parameters of a triple Langmuir probe with $r_p = 1.25\times10^{-4}$ m, $s = 10^{-3}$ m in a PPT plume.

Probe Parameters	Plasma Parameters			
	n_e=10^{19} (m^{-3}) T_e=2 eV, T_i=1 eV	n_e=10^{19} (m^{-3}) T_e=5 eV, T_i=1 eV	n_e=10^{21} (m^{-3}) T_e=2 eV, T_i=1 eV	n_e=10^{21} (m^{-3}) T_e=5 eV, T_i=1 eV
r_p/λ_D	38.2	24.2	382.1	241.7
s/d_S	300.9	190.3	3008.9	1903.0
$Kn_{C+,C+}$	3.3	11.5	0.044	0.15
$Kn_{F+,F+}$	3.3	11.5	0.044	0.15
$Kn_{F+,C+}$	3.1	10.9	0.041	0.14
$Kn_{e,C+}$	74.7	408.3	1	5.2
$Kn_{e,F+}$	74.7	408.3	1	5.2
λ_{ei}/λ_D	2856.2	9868.0	376.5	1250.7
$Kn_{e,e}$	52.8	288.7	0.7	3.7
τ_L	1228.4	409.5	12284.5	4094.8
	Neutral Parameters			
	$n_n = 10^{19}$(m^{-3}) $T_n = T_i = .5$ eV	$n_n = 10^{19}$(m^{-3}) $T_n = T_i = 1$ eV	$n_n = 10^{22}$(m^{-3}) $T_n = T_i = 5$ eV	$n_n = 10^{22}$(m^{-3}) $T_n = T_i = 1$ eV
$Kn_{C+,C}$	2792.1	3948.6	2.8	3.9
$Kn_{F+,F}$	4962.7	7016.9	5.0	7.0
$Kn^{CEX}_{C+,C}$	589.7	2113.1	0.59	2.1
$Kn^{CEX}_{F+,F}$	1574.3	5632.2	1.6	5.6

The formal evaluation of the uncertainty, ΔT_e , Δn_e, and $\Delta\phi_{s1}$ depends on the propagation of uncertainties of all the parameters entering into their evaluation as well as the non-linear coupling between them. We apply the methodology outlined by Gatsonis, et al [2002] for quadruple Langmuir probes but apply it to the triple Langmuir probe system of equations (2.14) and (2.17). However, the system of equations (2.14) and (2.17) are in implicit form and non-linear and therefore uncertainty analysis becomes somewhat more complex (see for example Coleman and Steele, 1999). To evaluate the absolute uncertainty we proceed by writing the system (2.14) and (2.17) in the form

$$
\begin{aligned}
f_1(T_e, n_e, \phi_{s1}, r_p, l_p, m_i) &= I_1 \\
f_2(T_e, n_e, \phi_{s1}, r_p, l_p, m_i, \phi_{12}) &= I_2 \\
f_3(T_e, n_e, \phi_{s1}, r_p, l_p, m_i, \phi_{13}) &= I_3
\end{aligned}
\quad . \tag{2.38}
$$

Upon differentiation the above system becomes

$$
\begin{aligned}
\frac{\partial f_1}{\partial T_e}\Delta T_e + \frac{\partial f_1}{\partial n_e}\Delta n_e + \frac{\partial f_1}{\partial \phi_{s1}}\Delta\phi_{s1} &= -\left(\begin{array}{l} \dfrac{\partial f_1}{\partial m_i}\Delta m_i + \dfrac{\partial f_1}{\partial l_p}\Delta l_p \\ + \dfrac{\partial f_1}{\partial r_p}\Delta r_p \end{array}\right) + \Delta I_1 \\
\frac{\partial f_2}{\partial T_e}\Delta T_e + \frac{\partial f_2}{\partial n_e}\Delta n_e + \frac{\partial f_2}{\partial \phi_{s1}}\Delta\phi_{s1} &= -\left(\begin{array}{l} \dfrac{\partial f_2}{\partial m_i}\Delta m_i + \dfrac{\partial f_2}{\partial l_p}\Delta l_p \\ + \dfrac{\partial f_2}{\partial r_p}\Delta r_p + \dfrac{\partial f_2}{\partial \phi_{12}}\Delta\phi_{12} \end{array}\right) + \Delta I_2 \\
\frac{\partial f_3}{\partial T_e}\Delta T_e + \frac{\partial f_3}{\partial n_e}\Delta n_e + \frac{\partial f_3}{\partial \phi_{s1}}\Delta\phi_{s1} &= -\left(\begin{array}{l} \dfrac{\partial f_3}{\partial m_i}\Delta m_i + \dfrac{\partial f_3}{\partial l_p}\Delta l_p \\ + \dfrac{\partial f_3}{\partial r_p}\Delta r_p + \dfrac{\partial f_3}{\partial \phi_{13}}\Delta\phi_{13} \end{array}\right) + \Delta I_3
\end{aligned}
\tag{2.39}
$$

The partial derivatives are the sensitivity coefficients and are obtained analytically. The non-linear system (2.39) is solved numerically for ΔT_e, Δn_e, and $\Delta\phi_{s1}$. The values used for the uncertainty coefficients are discussed below.

2.3.1 Uncertainty Coefficients

The TLP theory used assumes a single plasma species. Assuming the complete decomposition of Teflon® (PTFE), the ion mass is taken to be the weighted average of its constituents C and F. This equates to 16.667 amu. For this analysis the uncertainty in ion mass is taken to be zero. Any uncertainty due to the presence of multiple plasma species is not accounted for in the present analysis.

The uncertainty in the probe dimensions is $\Delta l_p = \Delta r_p = \pm 2.54 \times 10^{-5}$ m. This value is from the resolution of the calipers used to construct the probes. The calipers had a resolution of ± 0.001 in. The tungsten wires used to construct the probe were measured with these calipers to ensure that each wire was of the same length and diameter.

The uncertainty in the measured currents is obtained from the manufacturer of the current probes (Tektronix). The DC accuracy is given as ±3% of full scale, correctable to ±2% of full scale from 50 mA to 5A and ±1% of full scale from 5 A to 15 A when the probes are properly calibrated. A subroutine of the Fortran code used for data reduction determines what the uncertainty is for each probe current. This is done by first determining the maximum of each current. The assumption is made that the scope was set to maximize each current on half of the screen or within 5 divisions. The code determines what scope setting was used to fit the maximum current in 5 divisions and then calculates the full scale value using that setting. The full scale value is equal to 10 divisions times the current/division setting. The uncertainty is then taken as either ±2% or ±1% of the full scale value depending on the full scale value (greater than 5A is 1%, less than 5A is 2%). The calculated current uncertainty is also used as a filter to remove extraneous points from processing. Any values smaller than the uncertainty value are not processed.

Knowledge of the value of the bias voltages is essential in the analysis of TLP data both for the solution for T_e and n_e and also in determining the uncertainties in those quantities. The bias voltage was provided by common batteries. Two D-cell (1.5 V)

batteries in series were used for ϕ_{12} and two 9-V batteries in series were used to provide ϕ_{13}. The voltages could be measured before and after each pulse with a voltmeter. This however will only indicate whether any change has taken place to these batteries from the presence of the plasma interacting with the TLP circuit. Ideally the bias voltages should be recorded at every measurement location and PPT firing along with the probe currents. Then the time-dependent values of $\phi_{12}(t)$ and $\phi_{13}(t)$ could be used in the solution of system (2.14) and (2.17). In order to assess the variability of the bias voltages during the PPT operation the bias voltages at 20 cm on the centerline for each energy level were recorded. The data are shown in Figure 2.16, Figure 2.17, and Figure 2.18 for the 5-J, 20-J, and 40-J cases respectively.

The measurement of the bias voltage was done by using single ended voltage probes and measuring the voltage of each probe and then mathematically taking the difference to come up with the bias voltage value as a function of time. This technique introduces some uncertainty into the measurement due to the resolution of the oscilloscope. The oscilloscope used had a voltage signal resolution of 8 bits. This means that it divides the measurement range up into 256 discrete measurement levels. So for example with a range of 100 volts the minimum resolvable value is 0.39 volts.

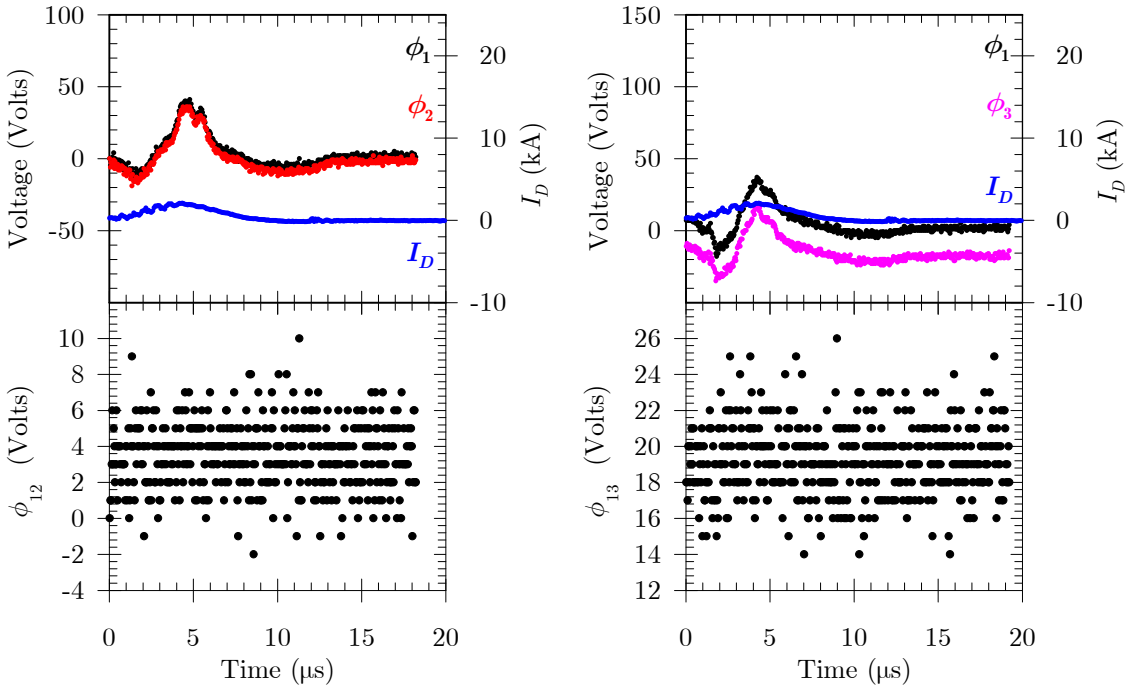

Figure 2.16 Applied voltage bias of a triple Langmuir probe during a 5 J laboratory PPT pulse.

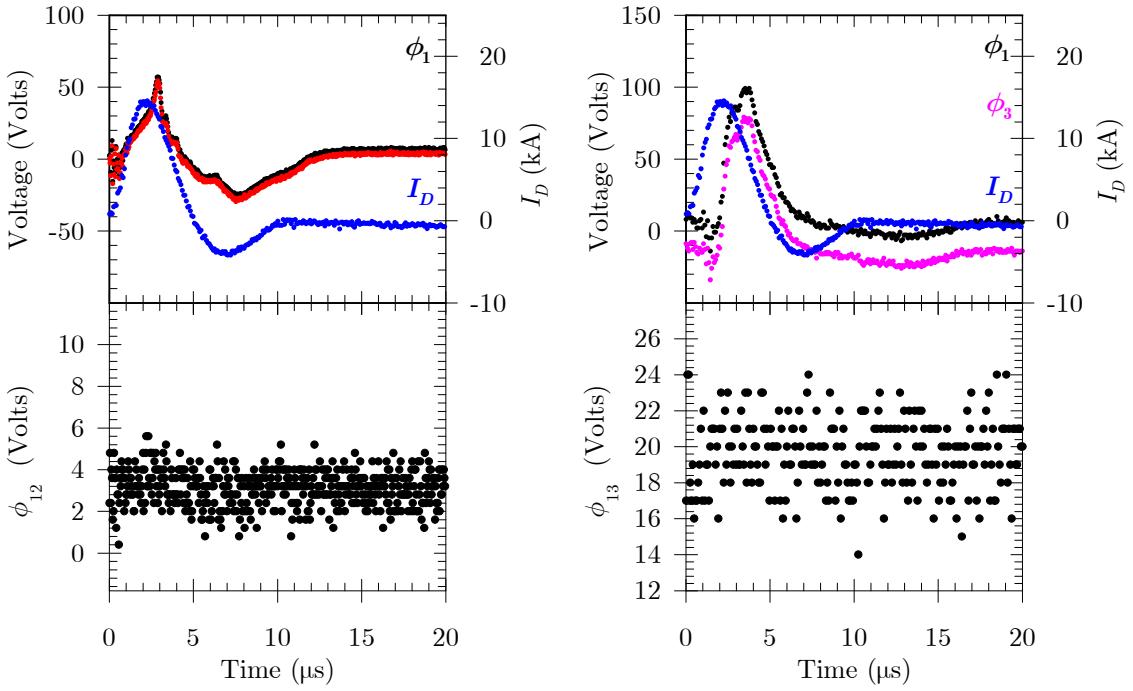

Figure 2.17 Applied voltage bias of a triple Langmuir probe during a 20 J laboratory PPT pulse.

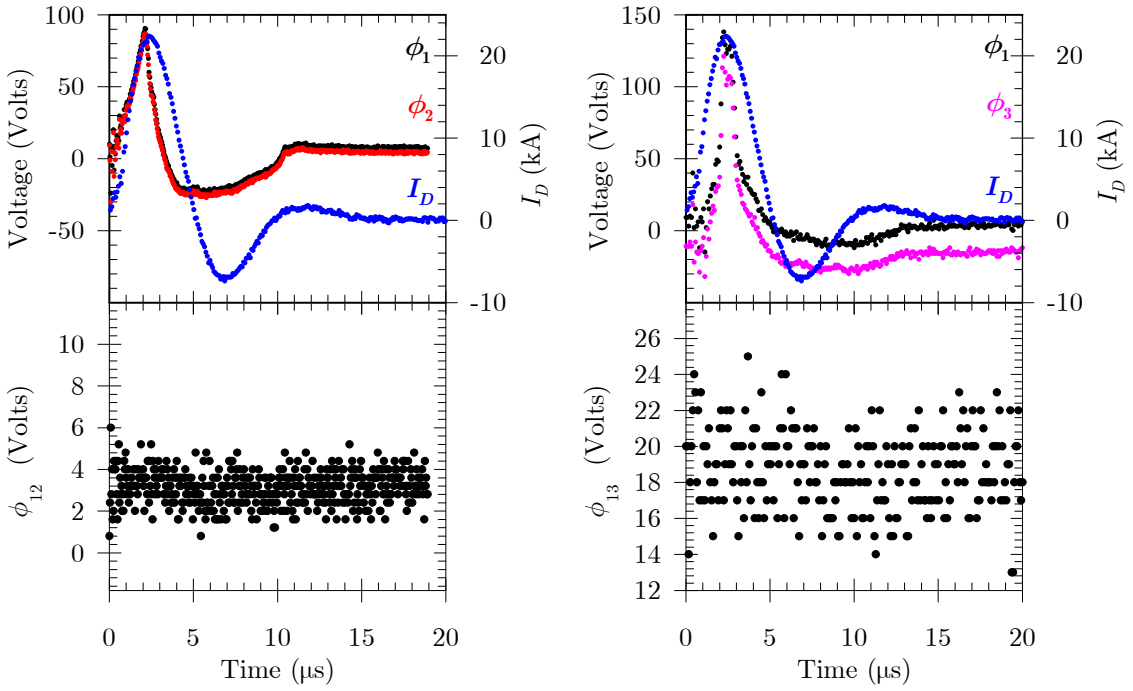

Figure 2.18 Applied voltage bias of a triple Langmuir probe during a 40 J laboratory PPT pulse.

During a pulse the voltages of ϕ_1 and ϕ_2 varied considerably from a peak of over 100 volts during the maximum probe current to values less than 10 volts near the end of the pulse. The dynamic range of the signal results in a resolution of less than 1 bit for V_{12} and V_{13}. This phenomenon is known as bit-rate error and can be seen in the noise or spread on ϕ_{12} and ϕ_{13} measurements. This is not however the only source for this spread, there is most likely other random error included within. Table 2.3 shows the sample mean $\bar{\phi} = \frac{1}{N}\sum_{i=1}^{N}\phi_i$, the standard deviation $S_\phi = \left[\frac{1}{N-1}\sum_{i=1}^{N}\left(\phi_i - \bar{\phi}\right)^2\right]^{\frac{1}{2}}$, and the 95%

confidence interval of the sample mean, given by, $\left(\bar{\phi} - \frac{tS_{\phi}}{\sqrt{N}}, \bar{\phi} + \frac{tS_{\phi}}{\sqrt{N}}\right)$ where t is the significance level. The sample is $N = 500$.

Table 2.3 Statistical values of the bias voltages for each energy level of the laboratory PPT.

	ϕ_{12}			ϕ_{13}		
Discharge Energy	Mean	Standard Deviation	95% Confidence Interval	Mean	Standard Deviation	95% Confidence Interval
E=05 J	3.4920	1.7867	0.1570	19.2100	1.9312	0.1697
E=20 J	3.1168	0.8607	0.0756	19.5200	1.9404	0.1705
E=40 J	3.1432	0.8305	0.0730	18.8840	2.0628	0.1813

The values for mean and 95% confidence interval of ϕ_{12} and ϕ_{13} for each energy level are then used as inputs into the data reduction algorithm for ϕ_{12}, ϕ_{13}, $\Delta\phi_{12}$, and $\Delta\phi_{13}$.

The major contributions to ΔT_e and Δn_e from the uncertainties on the right hand side of system (2.39) where found by computing ΔT_e and Δn_e with all uncertainty terms set to zero except one. The non-zero uncertainty term was taken as both positive and negative to prove that a full error bars are being predicted.

Figure 2.19 and Figure 2.20 show the results of this uncertainty analysis for two data sets that would represent the extremes of measurement. These measurements are taken at 10 cm from the Teflon® surface along the thruster centerline at an energy level of 5 and 40-J. The leftmost column in each figure shows the raw probe data (probe currents and discharge current) as well as plots of the reduced $T_e(t)$ and $n_e(t)$ values. To the

right of the $T_e(t)$ and $n_e(t)$ plots are the resulting uncertainty contributions. The first column shows $|\Delta T_e|$ and $|\Delta n_e|$ calculated with the following uncertainty terms, $+\Delta\phi_{12}, +\Delta\phi_{13}, +\Delta r_p, +\Delta L_p, +\Delta I_p$. The next column shows $|\Delta T_e|$ and $|\Delta n_e|$ using $-\Delta\phi_{12}, -\Delta\phi_{13}, -\Delta r_p, -\Delta L_p, -\Delta I_p$ for the uncertainty terms. As can be seen, the magnitudes of $|\Delta T_e|$ and $|\Delta n_e|$ are not affected by the sign of the uncertainty values.

The 'total' in Figure 2.19 and Figure 2.20 designates the error in $|\Delta T_e|$ and $|\Delta n_e|$ with all terms set either positive or negative as indicated. This analysis shows that the error in $|\Delta n_e|$ is dominated by the $\pm\Delta r_p$ uncertainty. The error in $|\Delta T_e|$ is dominated by $\pm\Delta I_p$ and $\pm\Delta\phi_{12}$. The last column in Figure 2.19 and Figure 2.20 shows the error with a combination of $\left(+\Delta\phi_{12}, +\Delta\phi_{13}, +\Delta r_p, +\Delta L_p, -\Delta I_p\right)$ or $\left(-\Delta\phi_{12}, -\Delta\phi_{13}, -\Delta r_p, -\Delta L_p, +\Delta I_p\right)$ for the uncertainty terms. This had a negligible affect on $|\Delta n_e|$ but served to maximize $|\Delta T_e|$. In Figure 2.21 we plot the error ΔT_e and Δn_e for the following combinations of uncertainty terms:

$\left(+\Delta\phi_{12}, +\Delta\phi_{13}, +\Delta r_p, +\Delta L_p, +\Delta I_p\right)$, $\left(-\Delta\phi_{12}, -\Delta\phi_{13}, -\Delta r_p, -\Delta L_p, -\Delta I_p\right)$,

$\left(+\Delta\phi_{12}, +\Delta\phi_{13}, +\Delta r_p, +\Delta L_p, -\Delta I_p\right)$, $\left(-\Delta\phi_{12}, -\Delta\phi_{13}, -\Delta r_p, -\Delta L_p, +\Delta I_p\right)$.

Figure 2.21 shows that when the sign of the independent uncertainties are changed, the sign of the total uncertainties is also changed.

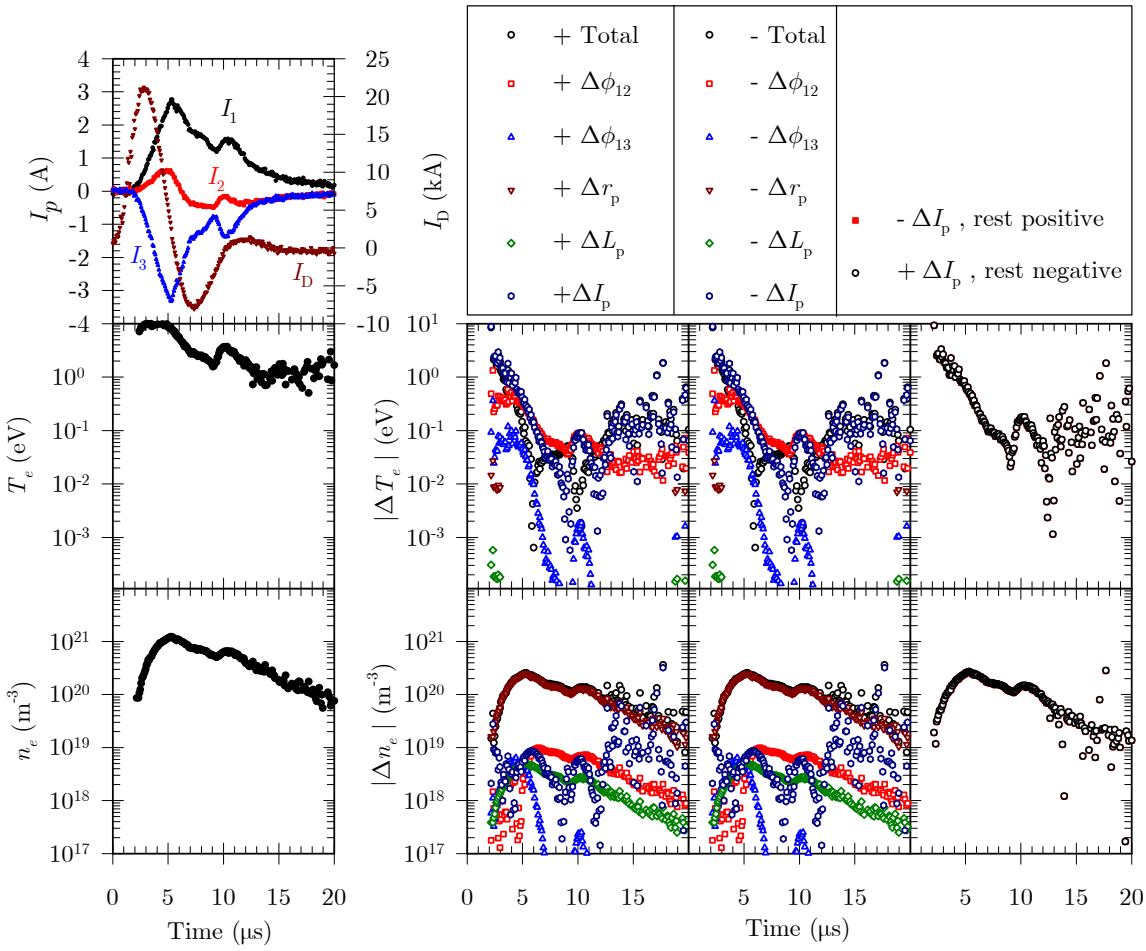

Figure 2.19 (Left) Probe currents, T_e and n_e for r=10 cm in the plume of a 40-J laboratory PPT. (Right) Error contributions to ΔT_e and Δn_e for various combinations of uncertainties.

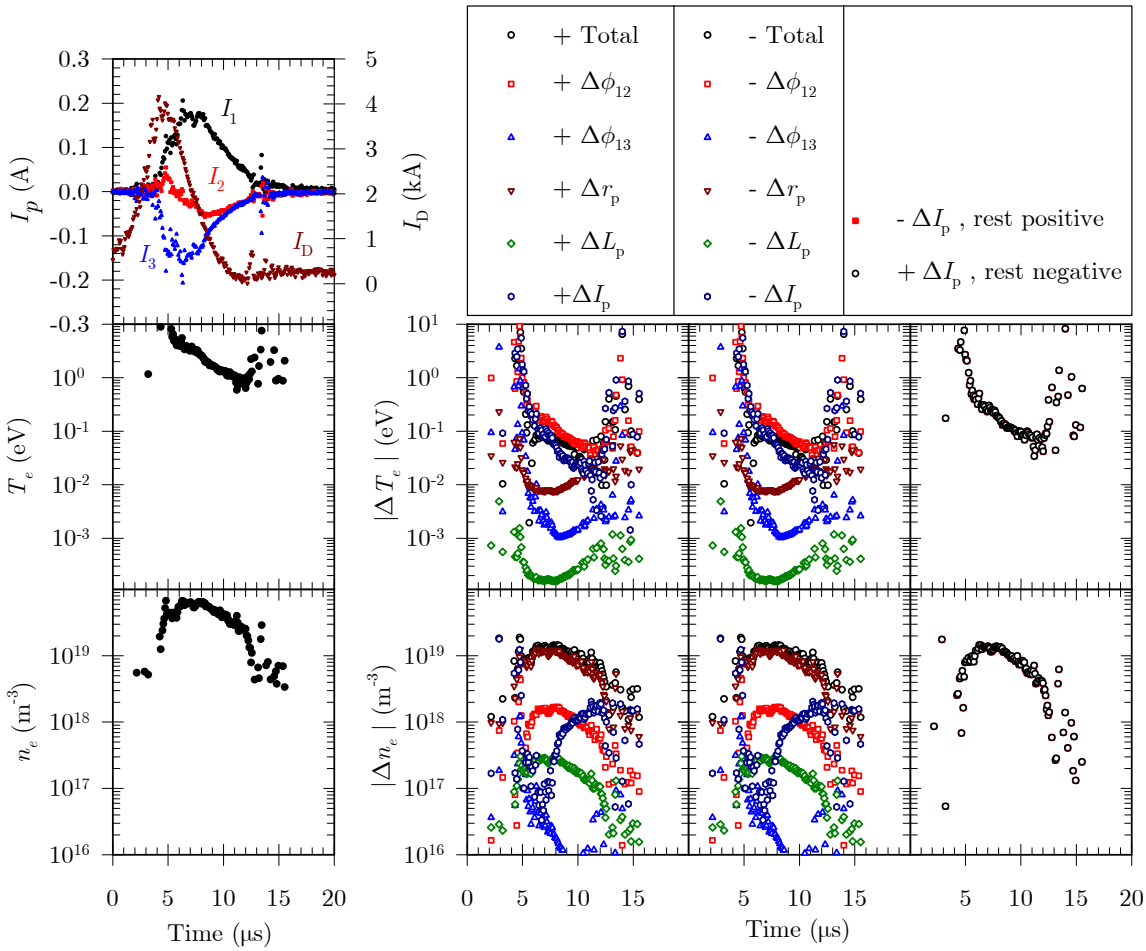

Figure 2.20 (Left) Probe currents, T_e and n_e for r=10 cm in the plume of a 5-J laboratory PPT. (Right) Error contributions to ΔT_e and Δn_e for various combinations of uncertainties.

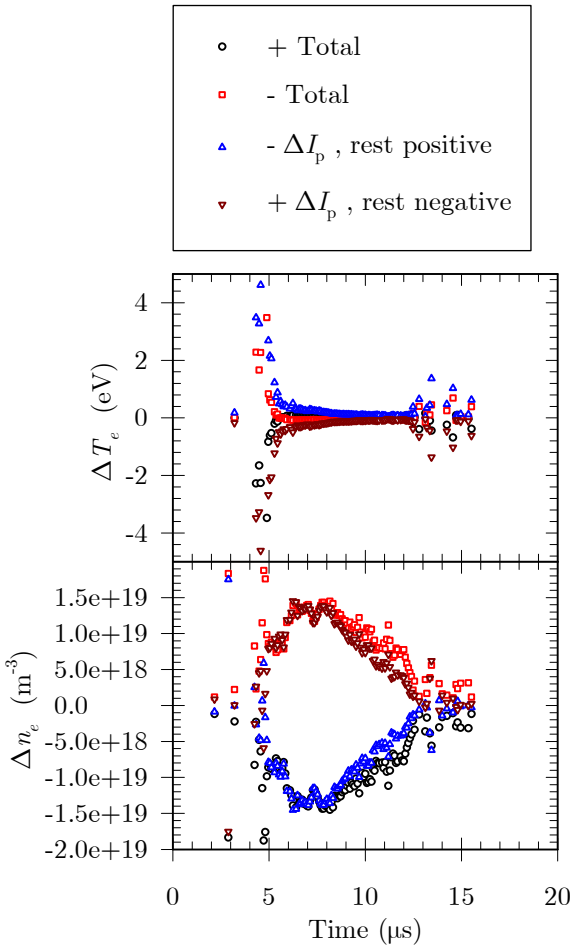

Figure 2.21 Error contributions to ΔT_e and Δn_e for various combinations of uncertainties at r=10 cm in the plume of a 5-J laboratory PPT.

2.4 Data Acquisition Procedures

Previous investigations using Langmuir probes noted degradation of signals after a number of shots [Eckman, 1999; Burton et al., 1999]. This could be eliminated by regularly cleaning the probes. However, if this could not be done within the vacuum environment it would cause a serious delay in the collection of data. Thus, the ability to clean the probes in-situ without breaking the vacuum of the facility was also essential.

2.4.1 Glow Cleaning

An important consideration in using probes in a plume is the possible adverse effects due to probe contamination [Guman and Begun, 1977]. After continuing operation of the PPT, the probes developed a dark film, possibly from decomposed Teflon® being deposited onto them. To eliminate this deposition an in-situ glow-cleaning method was used. This method used ion bombardment to clean off any buildup on the probes.

The glow cleaning procedure required the isolation of the oil-diffusion pumps. At the beginning of the procedure, the two gate valves over the oil-diffusion pumps were closed. Argon gas was then fed into the facility through a gas line attached to the probe-servo assembly (see Figure 2.5). The probes were then biased to a range of 1000-1200 V with respect to a nearby cleaning electrode by attaching the probe leads and the cleaning electrode leads to the high voltage power supply. When the pressure as read on one of the facility ion gauges reached a level around 3.0×10^{-4} torr the spark plug was fired several times. The excess electrons from the spark plug were needed to initiate a glow discharge between the probes and the cleaning electrodes. The current of the glow discharge was limited by the power supply to $\ll 100$ mA. The glow discharge was maintained for 30-60 seconds before the discharge ended on its own or the high voltage power was turned off. At this point the Argon gas was shut off and the gate valves to the oil-diffusion pumps were opened and the tank was brought back down to pressure.

From the start of the procedure to the point when the tank pressure has reached a level below 2.0×10^{-6} took only 15 minutes. This procedure was performed at the start of the testing and after every twenty to thirty firings of the PPT.

2.4.2 Measurement Locations

Measurements in the plume were performed in an attempt to develop a comprehensive mapping of the PPT plume in the near field region. An $\left(r,\theta_{\perp}\right)$ and $\left(r,\theta_{\parallel}\right)$ coordinate system was established with the origin coinciding with the geometric center of the surface of the Teflon® propellant. The probe motion system allowed angular measurements to span a full 180º. This range of motion was needed to explore the backflow regions in attempt to detect any tendencies for the plume to backflow. The centerline of the thruster was located at $\theta = 90^{\circ}$. Radial measurements were confined to $r \leq 20$ cm.

Off-axis thrust measurements and plume contamination diagnostics performed by Arrington, et al. (1999 and 2000) showed a significant off-axis component of the PPT plume. To further investigate this canting of the plume measurements were taken in two perpendicular planes. One plane is parallel to the PPTs electrodes while the other is perpendicular to the electrodes. The coordinates of these two planes are distinguished from each other by their angular measurement. The angular measurement in the parallel plane is denoted by $\theta_{\parallel}$ while $\theta_{\perp}$ denotes measurements in the perpendicular plane. Previous investigations of the PPT plume (Eckman, 1999) only investigated one side of the PPT centerline. As such, no conclusion as to the extent of the asymmetry could be drawn.

The actual locations of measurements were at radial points of $r = 10, 15, 20$ cm. Figure 2.22 and Figure 2.23 respectively show the perpendicular and parallel plane measurement locations. Angular measurements ranged between 50-130º.

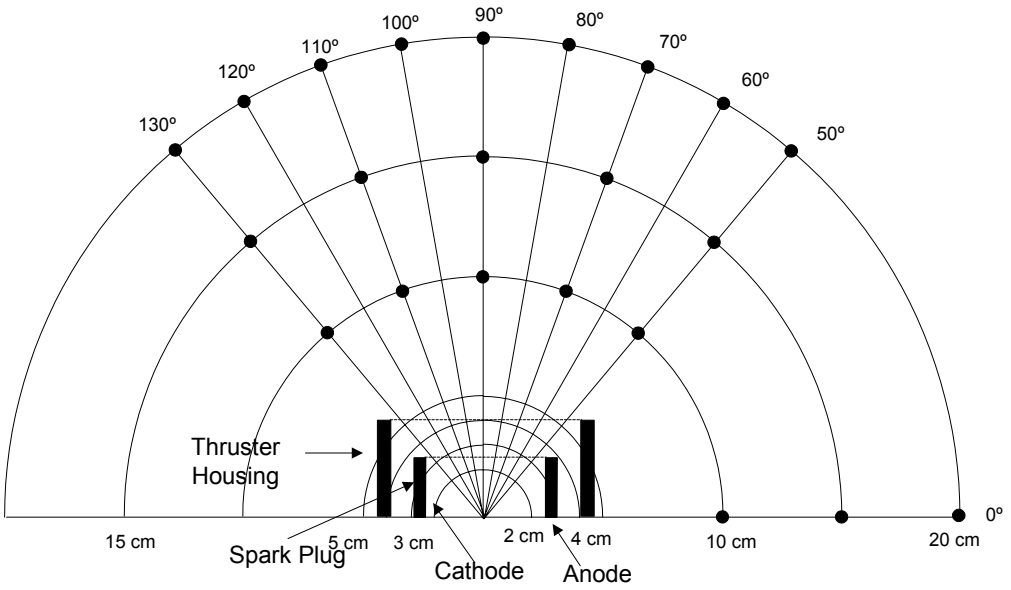

Figure 2.22 Langmuir probe measurement locations on the perpendicular plane $\left(r, \theta_{\perp}\right)$ of a laboratory PPT plume.

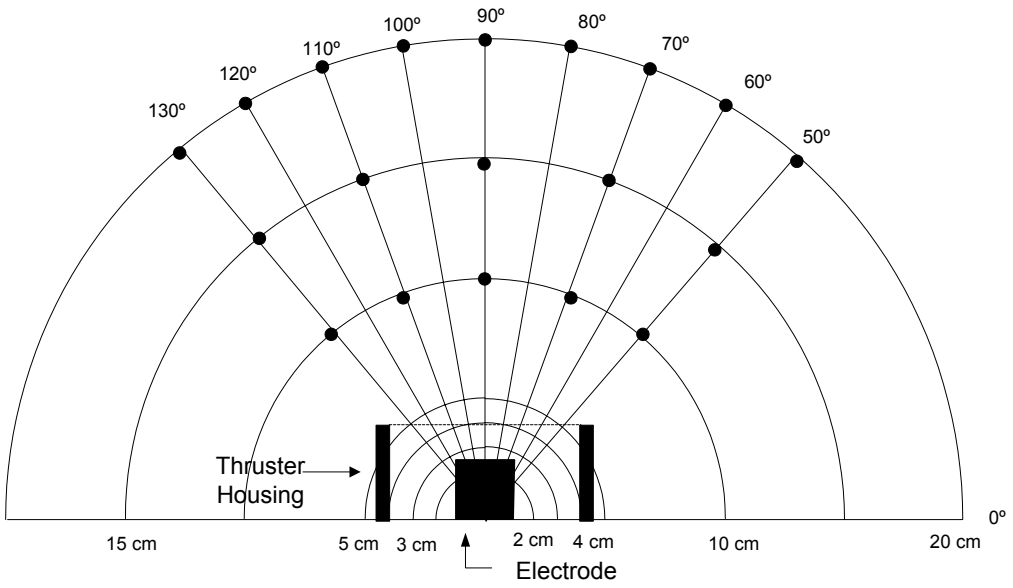

Figure 2.23 Langmuir probe measurement locations on the parallel plane $\left(r, \theta_{\parallel}\right)$ of a laboratory PPT plume.

Double probe measurements were only performed at three locations within the plume. These were $\left(r = 10\,\mathrm{cm}, \theta_{\perp} = 90^{\circ}\right)$, $\left(r = 10\,\mathrm{cm}, \theta_{\perp} = 70^{\circ}\right)$, and $\left(r = 4\,\mathrm{cm}, \theta_{\perp} = 90^{\circ}\right)$.

2.4.3 Triple Langmuir Probe Current Measurement Procedure

The short duration of the PPT pulse (~15-20 μs) requires a small time base be used to record data on the oscilloscope to achieve the best resolution. In order to only record the measurement signals during the period of interest a method was needed to initiate the acquisition of data. The previous investigation [Eckman, 1999] did not have a rigorous method to initiate data acquisition. The oscilloscope was set to begin recording

when it detected a signal from the probes that deviated above a set amount. This method captures only the absolute magnitudes of temperature and density at a particular point in the plume but does not give any information as to when things happen relative to the PPT discharge. To gain the most insight into the PPT plume the evolution of the temperature and density in relation to the PPT discharge is needed. To accomplish this, an event common to all the measurements is needed that can be used as a time zero (t=0 s). The obvious choice would be the actual firing of the PPT. For this purpose a Rogowski coil was imbedded into the main capacitor of the PPT. A Rogowski coil measures the time derivative of a current using the Hall Effect. The Rogowski coil in the main capacitor would be able to measure the discharge current of the PPT and could accurately identify the beginning of the PPT pulse.

The signal from the Rogowski coil was quite noisy however. As such, it alone was a poor reference point to use. To alleviate this an integrator was built which would integrate and filter the Rogowski coil's time derivative of the current into a current waveform. This current waveform of the PPT discharge was quite clean and consistent (Figure 2.24).

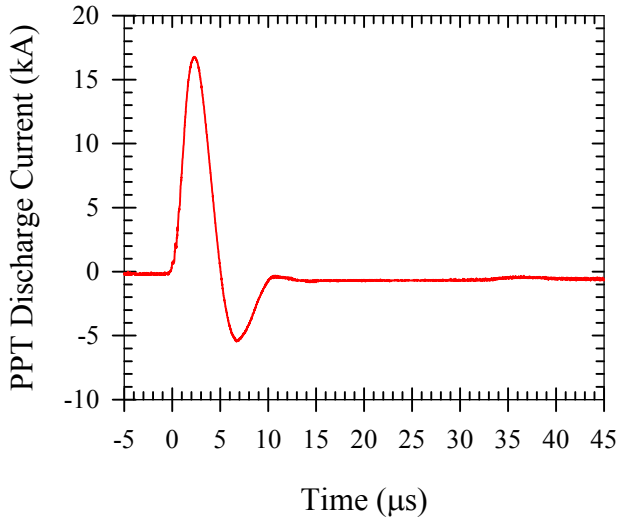

Figure 2.24 Discharge current of a 40-J laboratory PPT.

This integrated signal from the Rogowski coil was used to trigger the oscilloscope in order to begin the data acquisition sequence. The oscilloscope was set with a time base of 5 μs/division. This would mean that a total time window of 50 μs would be recorded which was adequate to see the entire pulse from the moment the main capacitor began to discharge until well after the plasma had passed by the probe.

The data of interest were the currents collected by each of the three probes, P_1, P_2, and P_3. These currents were acquired using Hall Effect current probes. Such current measurements are very low impedance and as such prevent noise from entering into the system. Previous investigations (Eckman 1999 and Gagne 2000) using TLPs in the voltage-mode required the measurement of the potential between probe 1 and probe 2. This high impedance measurement allows noise to easily enter the system. Both of those previous investigations identified significant signal-to-noise ratios especially at the beginning of the pulse and needed to employ smoothing algorithms. By taking only low

impedance current measurements with the current-mode TLP used in this experiment, we reduced the noise significantly. The noise was reduced enough so as the need for smoothing algorithms were not necessary even at the beginning of the PPT discharge.

The data was recorded as five shot averages on the oscilloscope allowing a better representation of the pulses. To determine whether five shots were enough to represent the PPT pulse, probe current waveforms were recorded over sixty individual pulses of the PPT. The current waveform from P_1 was used to compute the standard deviation at every time as a function of number of shots fired. This gave a standard deviation at every time during each pulse, from this a time-averaged standard deviation was found for the entire pulse. The mean of the standard deviation was then plotted versus the number of shots fired (n) (Figure 2.25). This plot shows that the mean standard deviation reaches a maximum around five shots and then slowly asymptotes down to a constant value somewhere around 25 to 35 shots. Factoring in the constraint of glow cleaning the probes and the limited amount of facility time available, five shots were used to statistically represent the shot to shot variation while allowing a large amount of data to be collected.

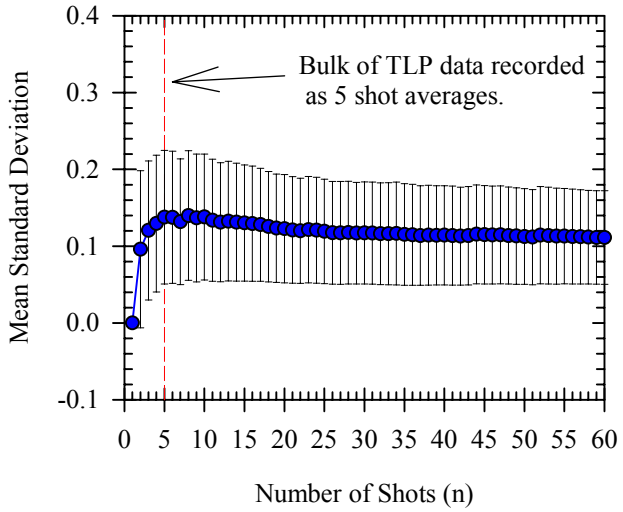

Figure 2.25 Mean standard deviation of the current from probe 1 vs. number of shots. The TLP was located at $\left(r = 10\,\text{cm}, \theta_{\perp} = 90°\right)$ in the plume of a 40-J laboratory PPT.

Each waveform was composed of 500 samples recorded over the 25 μs, this gives an effective sample rate of $2\text{x}10^7$ samples/s. The resulting averaged waveforms were stored onto a zip® drive from the oscilloscope in ASCII comma separated value form. After twenty to thirty total firings of the thruster, the glow cleaning procedures outlined previously were implemented. After the needed data were collected at a particular location, the probes were moved to a new location using the computer controlled probe motion system.

2.4.4 Double Langmuir Probe Measurement Procedure

For the double Langmuir probe data the bias voltage ϕ_b needed to be swept through a range of voltages, a difficult procedure for a time-varying plasma in a plume from a PPT

discharge that lasts $10-15\ \mu s$. To overcome the unsteady nature of the PPT plasma a way around the bias voltage sweep requirement needed to be developed. This was done by combining several PPT discharges into one. The applied voltage was swept at discrete levels in the range of ± 27 V. At each voltage level the PPT was discharged and the currents were measured as shown in Figure 2.26 for a typical case. As with the triple Langmuir probe data this data was also recorded as five-shot average waveforms.

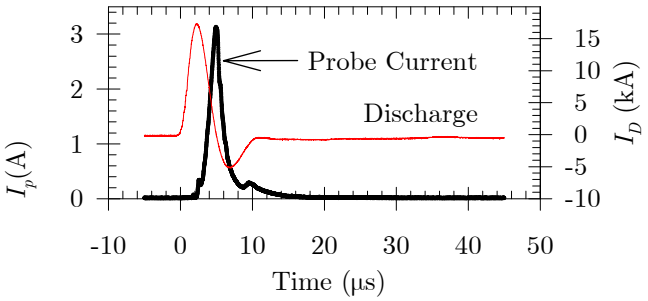

Figure 2.26 Typical double Langmuir probe current and PPT discharge current.

From these families of curves the value of the probe current was extracted at a common time across the range of bias voltages at each spatial location. From this procedure an *I-V* curve was compiled and was then fitted to the theoretical expression for the probe current, equation (2.31). Figure 2.27 shows a typical I-V characteristic curve and the resulting curve-fit to the experimental data. This was repeated at 0.5 μs increments until a family of I-V characteristics was created. This allowed the evaluation of the unsteady electron temperature and number density. Double probe data was acquired at two radial locations, $\theta_{\perp} = 70°$ and $\theta_{\perp} = 90°$, at an axial distance of $r = 10$ cm and discharge energy of 20 Joules.

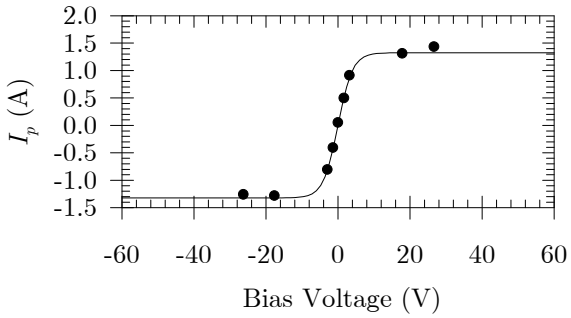

Figure 2.27 Typical double Langmuir probe *I- V* characteristic.

Chapter 3 Data Reduction, Analysis, and Discussion

In this chapter the Langmuir probe (double and triple) data analysis is presented. This is accomplished through the use of a computational algorithm developed to solve the necessary equations to provide $T_e(r,\theta,t)$ and $n_e(r,\theta,t)$.

3.1 Triple Langmuir Probe Data Reduction and Error Analysis

The triple Langmuir probe data is output from the oscilloscope as ASCII data. The raw output files from the oscilloscope are combined into one comma delimited text file containing the time, I_1, I_2, and I_3. This file is then passed into the data reduction algorithm that outputs a data file containing t, T_e, ΔT_e, n_e, Δn_e, ϕ_{s1}, and $\Delta\phi_{s1}$.

The data reduction algorithm was written in Fortran90 to solve the system of equations (2.14) and (2.17). It uses a globally convergent Newton's method to solve the non-linear set of equations. The data reduction algorithm follows the procedure outlined below.

- Import data file.
- Create output file.
- Find uncertainty value for measured probe currents based on maximum probe current.

- Calculate initial guess for T_e, n_e, and ϕ_{s1} using the thin-sheath explicit equations, (2.18) and (2.19). The solution is based on a hybrid algorithm that combines the Newton-Raphson method and the Bisection method to solve for T_e (see Press et al, 1992 and 1996).
- Pass initial guess values to full thin-sheath equation solver.
    - This solver uses the globally convergent Newton's method for Nonlinear systems of equations to solve the system (2.17).
- Calculate the ratio of probe radius over Debye length, $\frac{r_p}{\lambda_d}$.
    - If $\frac{r_p}{\lambda_d} \leq 100$ then the full corrected theory equation set is solved, (2.14) using the globally convergent Newton's method, with the thin-sheath values used as the initial guess.
    - If $\frac{r_p}{\lambda_d} > 100$ then the thin-sheath values are used as the final solution.
- Calculate error ΔT_e and Δn_e.
    - Solve the system of equations (2.39). Solution is obtained using the globally convergent Newton's method.
- Write results to output file and repeat process for all time values.

3.2 Double Langmuir Probe Data Reduction and Error Analysis

Traditionally double Langmuir probes are used on steady plasmas. This allows for the bias voltage to be swept continuously through a range of values while measuring the resulting current flowing through the probe system. From these measurements a plot of the current-voltage characteristic can be generated that should correspond to the theoretical shape. From this characteristic curve it is quite easy to extract the necessary values to calculate electron temperature and density.

However the PPT discharge produces an unsteady plasma, lasting 10-15 μs. This transient plasma makes it a complicated and difficult task to produce a voltage sweep in that time period. This was overcome by sweeping the bias voltage by discrete levels over the course of several pulses and constructing an I-V characteristic from several shots as discussed in the procedures section.

The generated I-V characteristics data was imported into the SigmaPlot® graphing program. A curve fit of the experimental data to the theoretical expression (see equation (2.31)) for a double Langmuir probe was performed. This curve fit provided values for ion saturation current (I_i^*) and electron temperature (T_e) along with the standard error of these parameters. The standard error is an estimate of the uncertainties in the estimates of the regression coefficients. The electron number density can be found from equation (2.35) using the value for ion saturation current. This was repeated at each 0.5 μs

increment to assemble a composite time dependent picture of the electron temperature and number density of the PPT plume.

3.3 Results and Discussion

A typical set of triple Langmuir probe measurements and the resulting electron temperature and number density along with their respective errors are shown in Figure 3.1 for $r = 10\,\mathrm{cm},\ \theta_{\perp} = 90°, \mathrm{and}\ E_D = 20\text{-J}$. The top plot in Figure 3.1 shows the measured current data for all three probes as well as the discharge current of the PPT. As evident by the discharge current trace, the discharge of the PPT main capacitor lasts for approximately 12 μs and peaks after 2-3 μs. The triple probes begin to register current approximately 2 μs after the discharge current begins to rise and continues to register current for nearly 20 μs. Probe-1 is seen to collect mostly electron current while probe-2 collects mostly ion current. Interestingly, probe-2 collects electron current for some part of the beginning of the PPT pulse and ion current for the latter portion of the pulse. Figure 3.1 shows also the calculated values of $T_e(t)$ and $n_e(t)$. The trends shown in Figure 3.1 are characteristic of the majority of the data. Initially the data shows the presence of high temperature electrons corresponding to the time of the peak discharge current. A secondary peak in electron temperature is also present as previously reported. The maximum electron temperature $T_e^{\max}(10,90) = 9.2\ \mathrm{eV}$ occurs near the peak in discharge current. The maximum electron density $n_e^{\max}(10,90) = 7.2 \times 10^{20}\ \mathrm{m^{-3}}$ occurs slightly after the maximum temperature. Eckman, et al. (1999 and 2001) reported similar observations of electron temperatures.

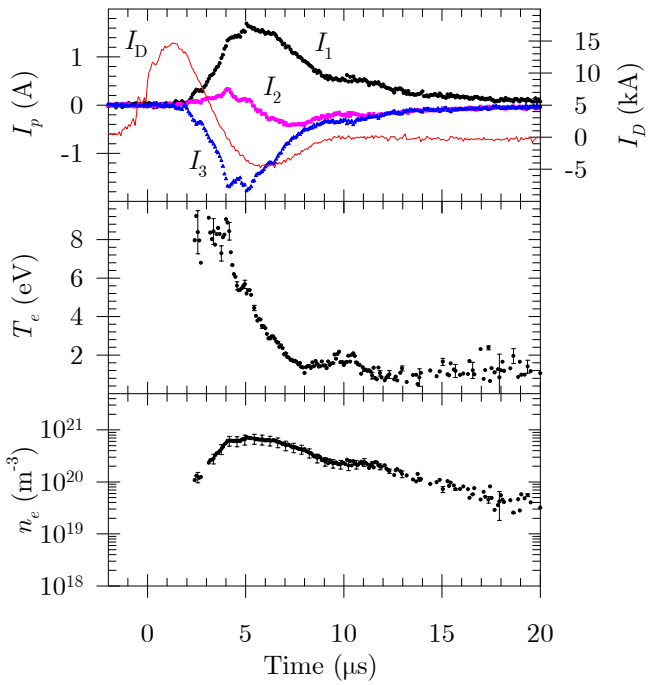

Figure 3.1 Triple Langmuir probe results at $\left(r = 10\,\text{cm}, \theta_{\perp} = 90°\right)$ in the plume of a 20-J laboratory PPT. Top plot shows TLP currents and PPT discharge current. Next two plots show $T_e(t)$ and $n_e(t)$.

The data reported in Byrne, et al. (2000) and Eckman, et al. (1999 and 2001) was collected using the voltage-mode TLP technique. The data there required a voltage measurement that became corrupted by significant amounts of high frequency noise during the first 10-12 μs. The plasma from the laboratory PPT used in all of these experiments including this thesis only remains dense enough to obtain TLP data for ~15-20 μs. The raw data was processed using a Loess smoothing algorithm. This allowed for processing of the data without numerical instabilities, though data for the initial portion of the plume is somewhat questionable. The current-mode TLP technique used for this thesis reduced the amount of noise in the beginning portion of the data, this allowed for better insight into the presence of higher temperature electrons at the beginning of the

pulse. The smoothing algorithm used previously reduced the magnitude of the initial electron temperature. However, even with the current-mode TLP technique we are still not able to resolve the electron temperature during the first two microseconds or so and most likely the true peak electron temperature.

Double probe data taken at two spatial locations is shown in comparison with the corresponding locations for triple probe data in Figure 3.2. The data was taken at $r = 10$ cm and at $\theta_{\perp} = 70° \text{ and } 90°$. The laboratory PPT was operated at a discharge energy of 20-J for these data points. As can be seen there is good agreement between the two Langmuir probe techniques. Both techniques showed the presence of high temperature electrons at the beginning of the pulse. This was followed by a peak number density on the order of $n_e = 10^{21} \text{m}^{-3}$ with electron temperatures quickly dropping to below $T_e = 2$ eV for the remainder of the pulse. The characteristic secondary peak in electron temperature was present in both Langmuir probe techniques around 10 μs. This secondary peak corresponds with the secondary peak in the PPT discharge current.

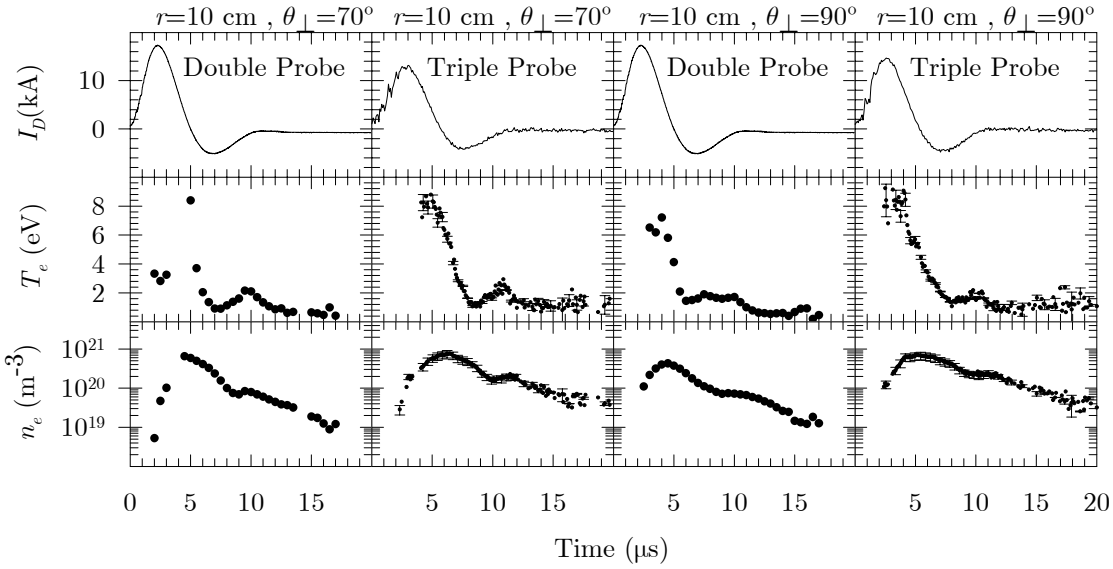

Figure 3.2 Comparison between double and triple Langmuir probe results at locations of $\left(r = 10\,\text{cm}, \theta_{\perp} = 70° \text{ and } 90°\right)$ in the plume of a 20-J laboratory PPT. The top row shows the 20 J laboratory PPT discharge current while the next two rows show electron temperature and density of the plume.

Figure 3.3 through Figure 3.8 present the triple probe data for a 5-J, 20-J and 40-J energy respectively for distances $r = 10$ cm, $r = 15$ cm, and $r = 20$ cm on both the perpendicular and parallel planes. Figure 3.3, Figure 3.5, and Figure 3.7 show data on the parallel plane and Figure 3.4, Figure 3.6, and Figure 3.8 the perpendicular plane.

The triple Langmuir probe parallel plane data from a 5-J laboratory PPT is shown in Figure 3.3. This figure is a collection of the entire parallel plane data presented in such a way as to make any angular or radial trends evident. It is grouped into three sections of three rows each that correspond to the three radial distances explored. The top three rows portray the $r = 10$ cm data with each column across representing the angular probe location. The first row in the grouping begins with the 5-J laboratory PPT discharge current at each angular location. The next two rows display the electron temperature and

number density at each angular location. The next grouping of three rows located in the middle of the figure is for the $r = 15$ cm data. It is organized in the same fashion, of discharge current followed by electron temperature and then number density. The final grouping of three rows is for the $r = 20$ cm data, and is arranged the same as the previous two groupings. If one follows a particular column down from the top of the figure a comparison of measurements at a constant angle can be compared to radial distance. The blank plots with the wording "No Data" are locations where raw data files had been corrupted or otherwise damaged so as to be unusable.

The parallel plane data for the 5-J energy level (Figure 3.3) is sparsely populated due to the raw data being recorded over a longer total time scale than the rest of the data. This resulted in very few usable data points during the actual PPT plume impingement on the triple Langmuir probe. Also the plume current densities are so low at the 5-J energy level, that the current collected by the triple probe is near the lower limit of the current probes resolution. There exists in most PPTs some variation from shot-shot in the exhaust plume. This laboratory thruster exhibits significant shot-to-shot variation particularly at the 5-J energy level. This is evident by the variation in discharge current waveforms in Figure 3.3 which are 5-shot averages.

Very little in the way of trends can be found in Figure 3.3 due to the small amount of reducible data points. In a broad sense it can be seen that the electron number densities remain below 10^{19} m^{-3} for all locations except for the $\left(10\,\mathrm{cm}, 90°\right)$ which appears to have a maximum electron number density below 10^{20} m^{-3}. The electron temperatures appear to be the highest along the centerline locations. For all locations though the electron temperature remains below 4 eV.

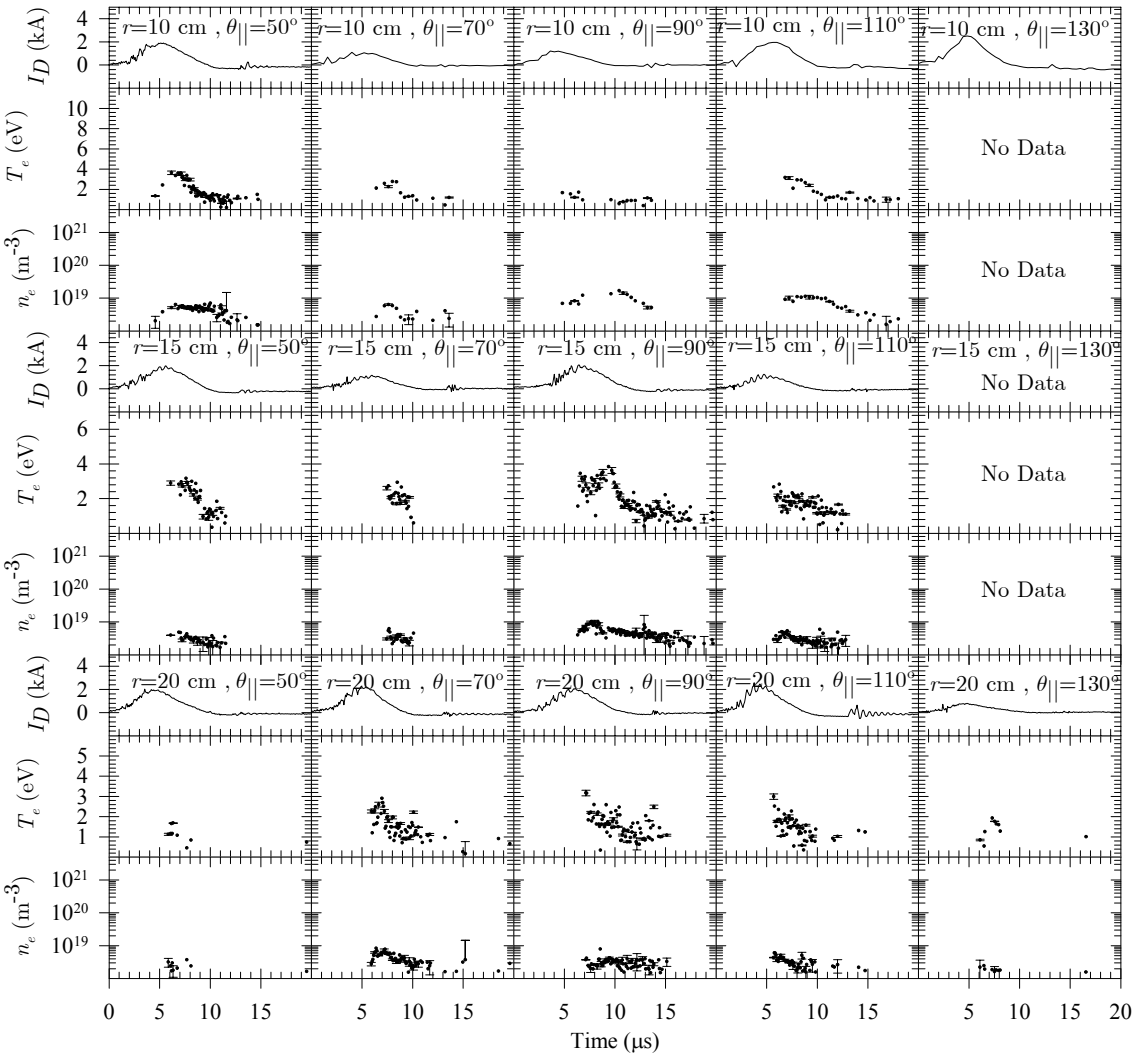

Figure 3.3 Triple Langmuir probe results on the $\theta_{\parallel}$ plane of a 5-J laboratory PPT.

Figure 3.4 presents the results of the triple Langmuir probe data for the perpendicular plane from a 5-J laboratory PPT. The figure is laid out in the same arrangement as Figure 3.3. There were more reducible data points at the locations on the perpendicular plane as the oscilloscope was configured to collect data at a higher fidelity. The current densities of the plume are still near the lower end of the triple Langmuir

probe's resolutions for this discharge energy level. The data is therefore a little sparse at the radial locations of 15 and 20 cm.

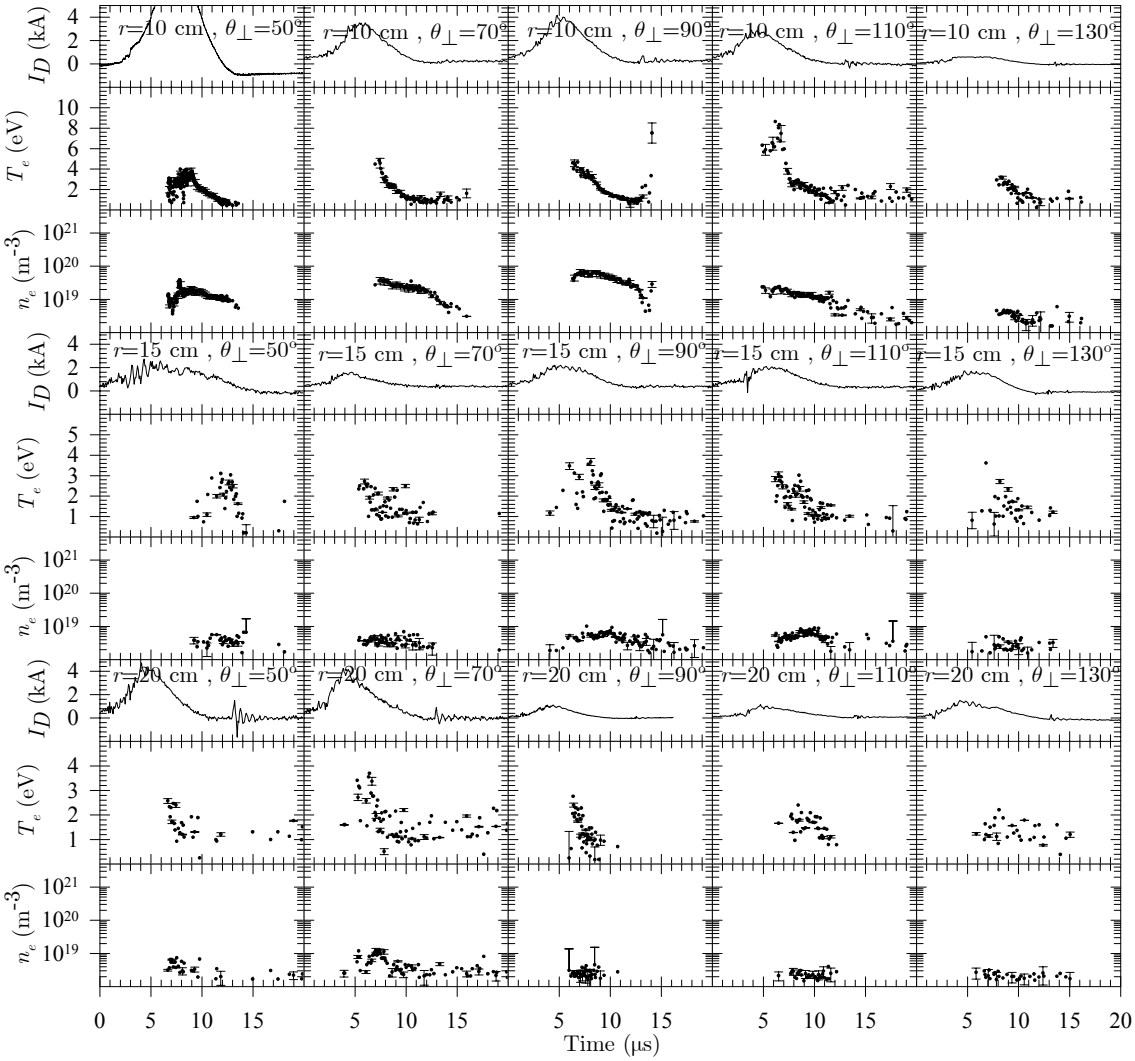

Figure 3.4 Triple Langmuir probe results on the $\theta_{\perp}$ plane of a 5-J laboratory PPT.

The top grouping of three plots in Figure 3.4 shows the 10 cm radial locations, this data seems to have the best resolution or most reducible data points for this measurement plane and discharge energy level. The maximum electron temperature here remains below 4-5 eV for all angles. It looks as if for the centerline areas the reducible

data only shows the decline in electron temperature during the second half of the discharge. This most likely means that the peak electron temperatures were not resolved and probably occurred during the initial plasma wave when the electron densities were low.

The number densities reach a maximum for the $\left(10\,\mathrm{cm}, 90^\circ\right)$ location that peaks around $10^{20}\,\mathrm{m}^{-3}$. The electron density declines to either side of centerline and as the probes are moved further downstream. By the 20 cm position the electron densities are peaking in the low $10^{18}\,\mathrm{m}^{-3}$ and for most of the plume are below the resolution of the probes or indistinguishable from the background densities. It appears that at the 20 cm location the plume has expanded somewhat so that the centerline location is less dense than to either side. This may however just be an artifact of the low fidelity of the measurements at 5-J.

The triple Langmuir probe results for the parallel plane of a 20-J laboratory PPT are shown in Figure 3.5. The graphic is arranged in the same format as the 5-J plots of Figure 3.3 and Figure 3.4 with three groupings of plots for each radial location of PPT discharge current, electron temperature, and electron number density. Again present in these plots are the presence of shot-to-shot variations showing up in the discharge current average waveforms. For the most part the discharge current averages have a peak current of approximately 10-12 kA, with a total discharge period of about 10-12 μs.

Evident from the plots in Figure 3.5 is the fact that the electron temperature is generally higher for the 10 cm radial locations with the peak values along the centerline. At the $\left(10\,\mathrm{cm}, 90^\circ\right)$ location a peak in the electron temperature can be seen occurring

between 3-4 μs with a peak value of about 11 eV. A secondary peak in electron temperature for this location appears at about 10 μs with a 2 eV magnitude. This secondary peak in electron temperature is noticeable to a certain extent at most of the locations in Figure 3.5.

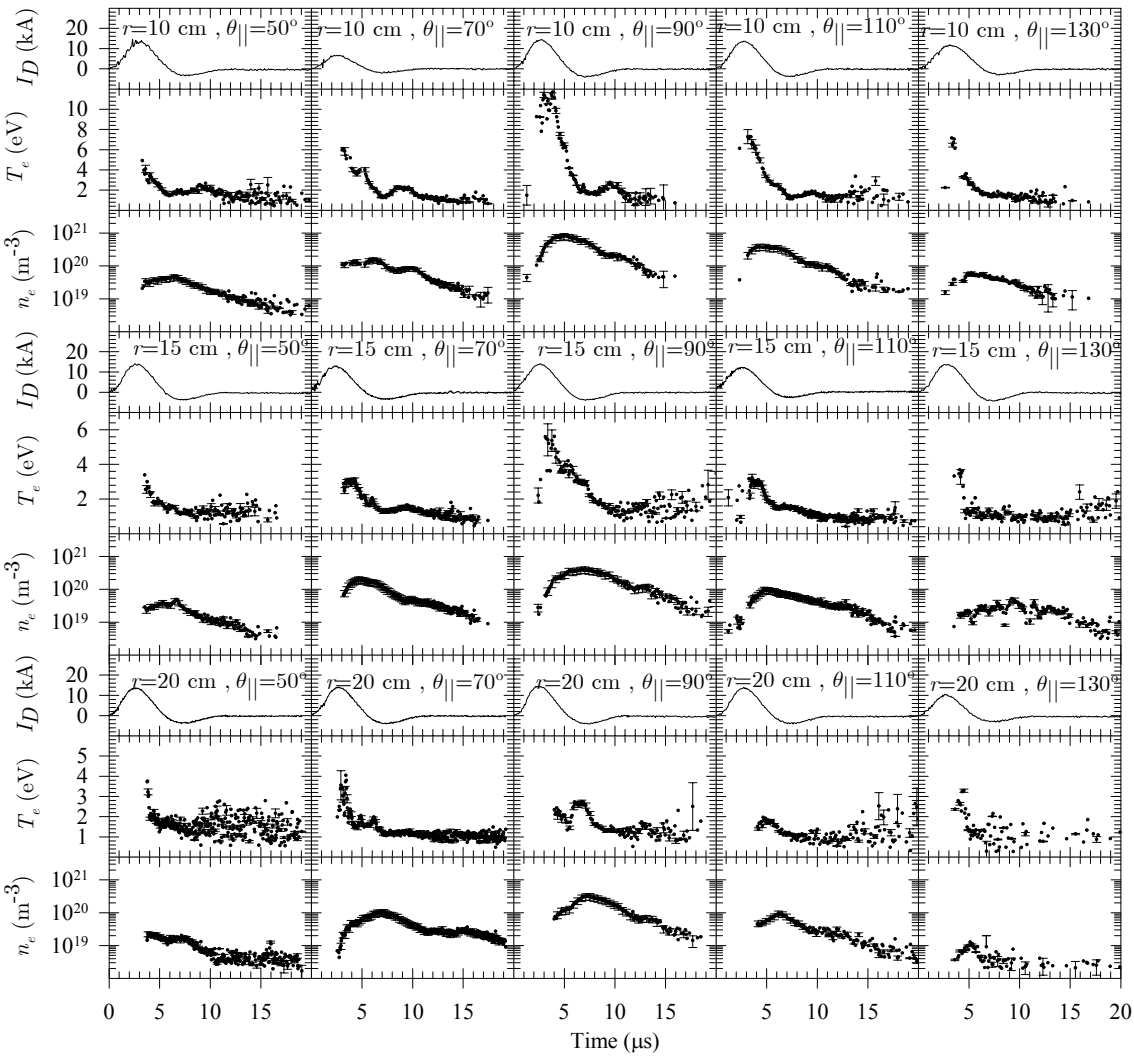

Figure 3.5 Triple Langmuir probe results on the $\theta_{\|}$ plane of a 20-J laboratory PPT.

The electron number densities portrayed in Figure 3.5 shows that the largest densities lie along the thruster centerline and decline as the plume travels downstream. The density also declines from its centerline values as the probe is moved to the sides.

The density is at a peak value for the $\left(10\,\mathrm{cm}, 90^\circ\right)$ location, where its peak value is near 10^{21} m^{-3}.

Figure 3.6 presents the triple Langmuir probe data from the perpendicular plane of a 20-J laboratory PPT. The graphic follows the same format as the previous plots. Three locations on this plane lacked reducible data unfortunately, and are labeled as 'No Data' in the figure. The data for locations $\left(20\,\mathrm{cm}, 70^\circ, 90^\circ \text{ and } 110^\circ\right)$ are different in appearance from the rest of the data because for these locations the oscilloscope was recording data at a higher sample rate. The $\left(20\,\mathrm{cm}, 110^\circ\right)$ location the measurement appears rather uncharacteristic as compared to all other waveforms taken. This could be the symptom of a contaminated probe. Although there were not many reducible measurement locations for the 20-J perpendicular plane, this measurement was left in the data set. Though, it is not believed to be representative.

As was the case with the parallel plane data of Figure 3.5, the perpendicular plane data of Figure 3.6 shows the electron temperatures to be consistently higher at the closest positions to the PPT. The peak electron temperature at the $\left(10\,\mathrm{cm}, 90^\circ\right)$ location peaks around 3-4 μs at a value of around 8-9 eV. The electrons quickly cool as the probe is moved downstream of the PPT to the 20 cm locations where the electron temperature is consistently below 4 eV for all angular locations.

The electron number densities are the highest as well near the PPT. The electron number density peaks at a magnitude of 10^{21} m^{-3} at the location of $\left(10\,\mathrm{cm}, 90^\circ\right)$. The time of this peak is approximately 5 μs. As the probe is moved downstream the densities

characteristically decline as well as when the probe is moved to the sides of the plume. The peak values at $\left(20\,\mathrm{cm}, 90^\circ\right)$ have declined an order of magnitude to $10^{20}\,\mathrm{m}^{-3}$.

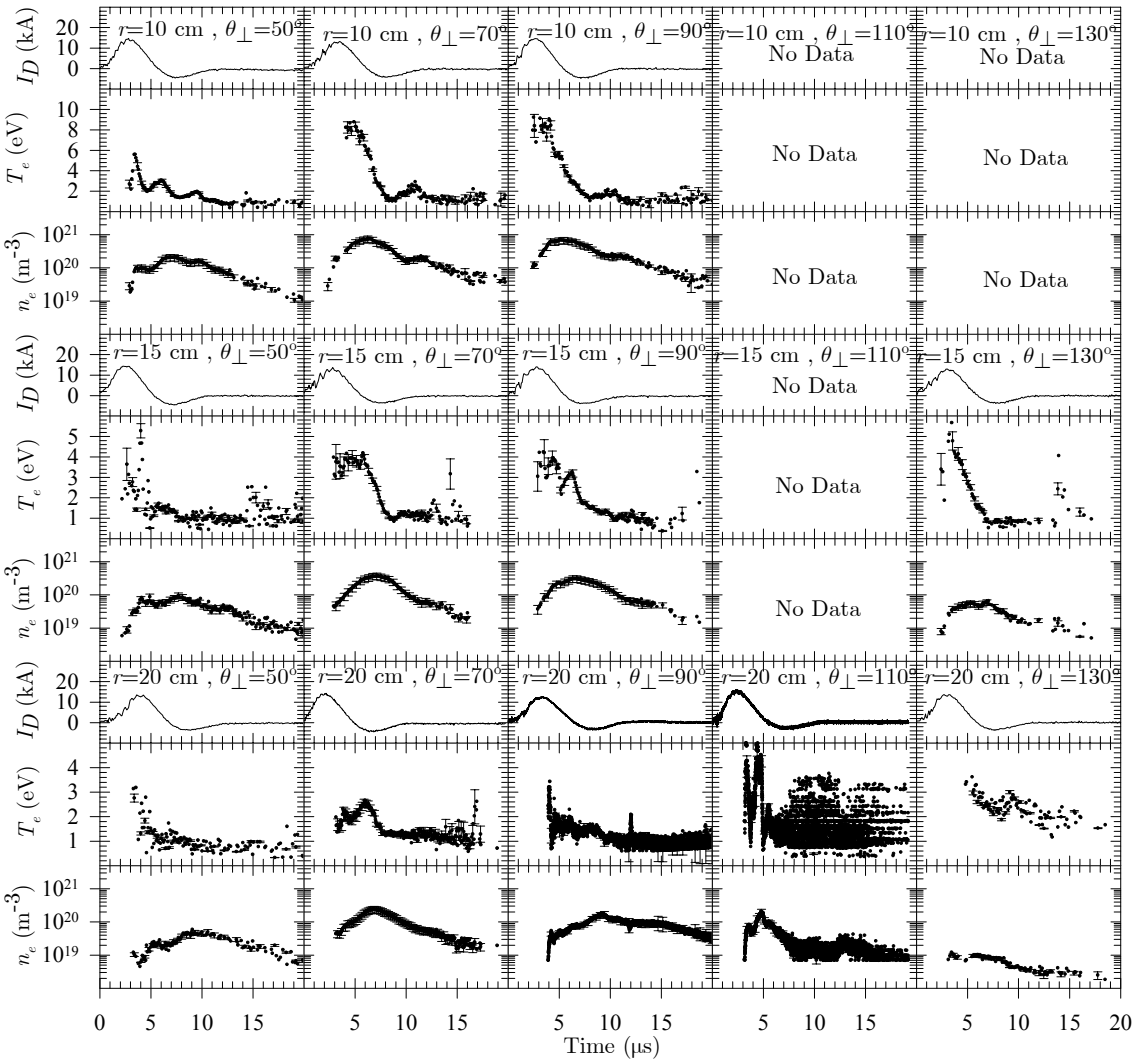

Figure 3.6 Triple Langmuir probe results on the $\theta_\perp$ plane of a 20-J laboratory PPT.

In Figure 3.7 the triple Langmuir probe results are presented for the parallel plane case of a 40-J laboratory PPT. This figure follows the same format as the previous cases. Characteristic of the discharge current plots for the 40-J discharge energy level are peak

currents of 20 kA occurring between 3-4 μs with a discharge period of 10-12 μs. A significant current reversal is evident of nearly 10 kA occurring around 7-8 μs.

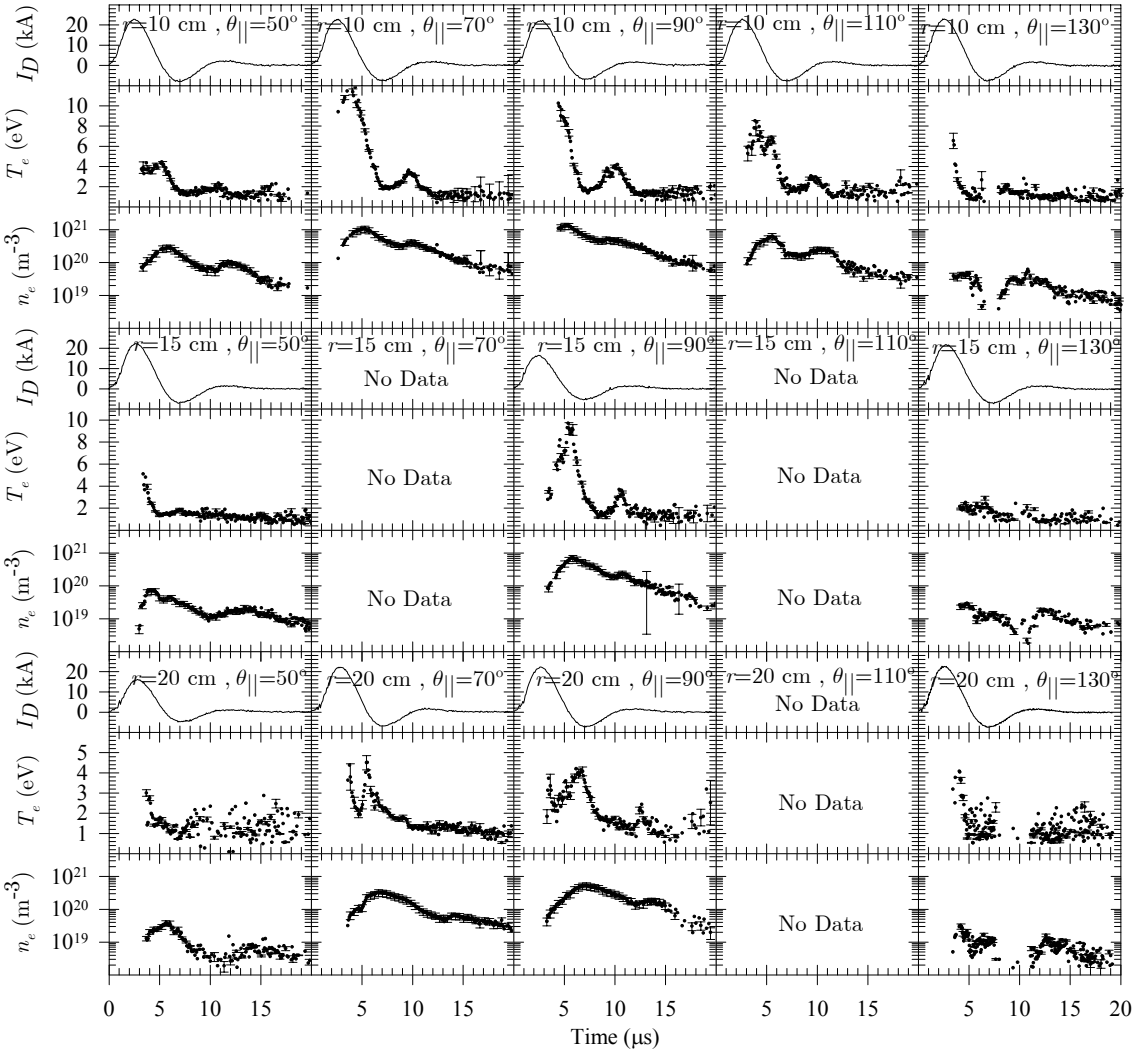

Figure 3.7 Triple Langmuir probe results on the $\theta_{\|}$ plane of a 40-J laboratory PPT.

The plots of electron temperature in Figure 3.7 have similar characteristics to the plots of the 5 and 20-J data. The temperatures are highest nearest the thruster and along the centerline. The peak in electron temperature for the $\left(10\,\mathrm{cm}, 90°\right)$ location is about 10

eV occurring at about 4-5 μs. No crest is evident in this data so it is likely that the actual peak in electron temperature could be higher at this point. The EMI from the 20 kA arc is most likely overwhelming to the electronics at this close of a location along the centerline. Interestingly the peak electron temperature at the $\left(15\,\mathrm{cm}, 90°\right)$ location is around 10 eV as well, much higher than the 5 and 20-J cases for this point. Clearly the plasma remains at an elevated temperature further from the PPT at the higher discharge energy levels. The characteristic secondary peak in electron temperature is evident in the centerline data here as well. This secondary peak appears to occur around the time of the second positive discharge current oscillation.

The electron number density again peaks along the PPT centerline close to the thruster as with the 5-J and 20-J. The highest electron number density occurs at the $\left(10\,\mathrm{cm}, 90°\right)$ location. The peak is about 10^{21} m^{-3} and occurs near the beginning of the reducible data at about 5-6 μs. The electron density remains near this value all the way downstream to the $\left(20\,\mathrm{cm}, 90°\right)$ location but occurs at a slightly later time of about 6-7 μs. The peak electron number density values in the far off-axis position at the $\left(20\,\mathrm{cm}, 50°\right)$ location remains relatively high, on the order of 10^{19} m^{-3}.

Figure 3.8 presents the triple Langmuir probe results for the perpendicular plane of a 40-J laboratory PPT. This figure follows the same format as the previous results. The electron temperature appears to be highest on the centerline at the nearest position to the PPT. The peak electron temperature is about 10 eV at the $\left(10\,\mathrm{cm}, 90°\right)$ location

occurring at about 4 μs. The peak electron temperature at the $\left(20\,\mathrm{cm}, 90^\circ\right)$ location is about 4 eV occurring at 7 μs.

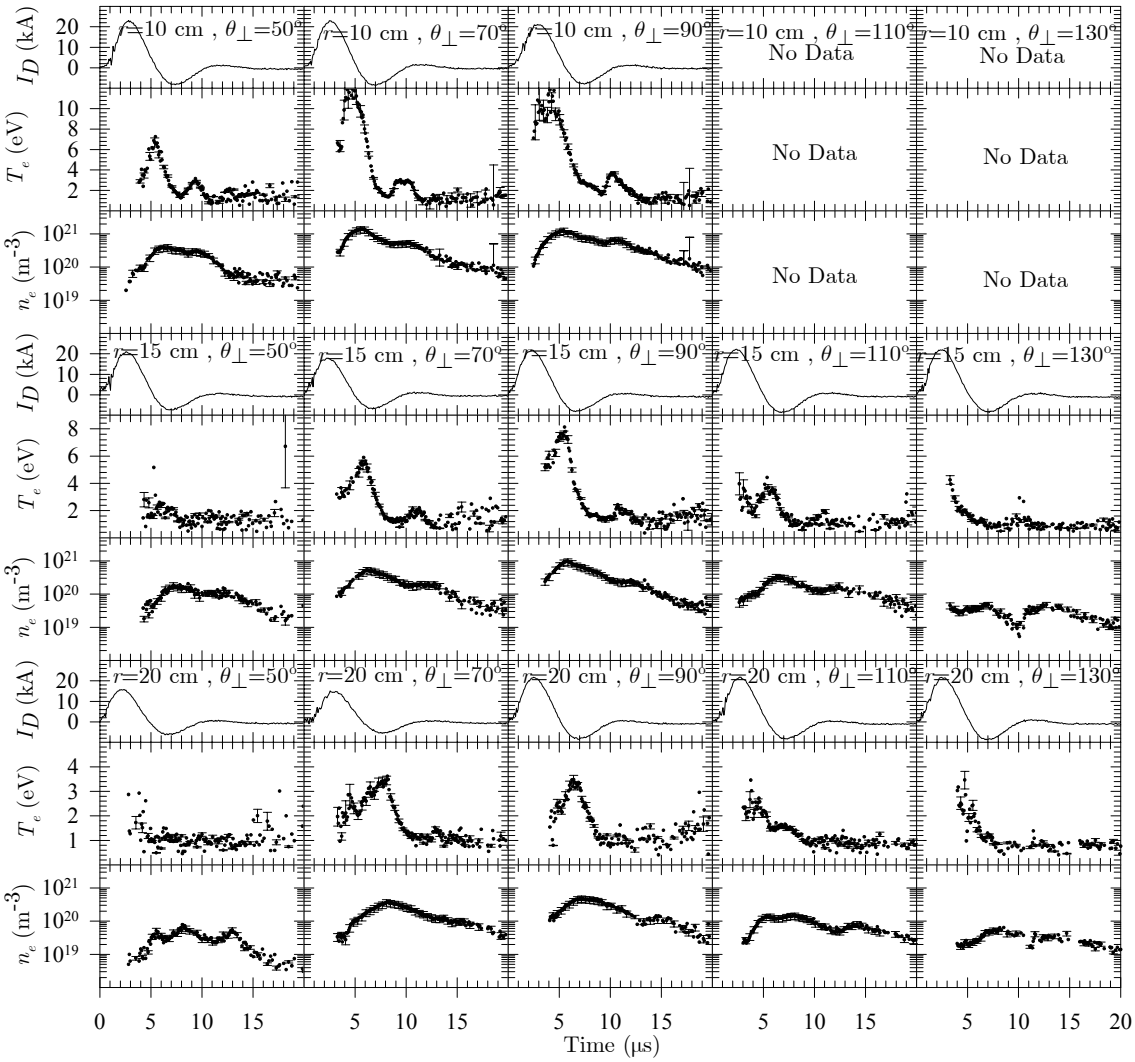

Figure 3.8 Triple Langmuir probe results on the $\theta_\perp$ plane of a 40-J laboratory PPT.

The electron number densities peak as well at the centerline position closest to the thruster. Much like all the previous results they decline in peak magnitudes as the probe is moved further off-axis and away from the PPT. Though much like the 40-J parallel plane case the electron number densities remain nearly the same all the way out to the 20 cm probe positions.

The electron temperature shows almost no angular dependence at any of the energy levels or measurement planes. The overall electron temperature decreases as the probe is moved further from the Teflon® surface. Electron temperature increases as a function of discharge energy level. Consistent across all the data is the presence of energetic electrons (about 10 eV) occurring during the PPT discharge. The electron temperatures quickly drop below 2 eV after the discharge current reaches zero. The second portion of the pulse contains relatively low energy electrons that remain present for 5-10 μs after the discharge has extinguished.

The electron density shows a reduction in magnitude with increasing angle from the centerline $(\theta = 90^\circ)$ and with distance downstream. The peak of the density consistently occurs after the electron temperature peaks for all of the data. The density peak occurs slightly later in time for the 20 cm data then the 10 cm data.

Figure 3.9 summarizes the peak values of electron temperature and number density of a 5-J laboratory PPT. The four plot figure is arranged in the following way. The first row contains the two plots for electron temperature, the left-hand plot the parallel plane data and the right-hand plot the perpendicular plane data. The second row contains the peak values of electron number density in a similar fashion. The plots show the maximum value as a function of angular location for each radial position. No angular dependence trend can be surmised from the electron temperature plots. The peak electron number density plots show a clear trend. The electron number density values peak along the PPT centerline $(\theta = 90^\circ)$ and decrease in magnitude to either side of the PPT centerline. The parallel plane plot does not show much difference between radial distances. This is due to the poor data resolution for parallel plane 5-J data. For the

perpendicular plane it can be seen that not only do all the values peak at the centerline but that the $\left(r = 10\,\mathrm{cm}\right)$ location is significantly larger than the other two. The points further downstream tend to fall on top of each other.

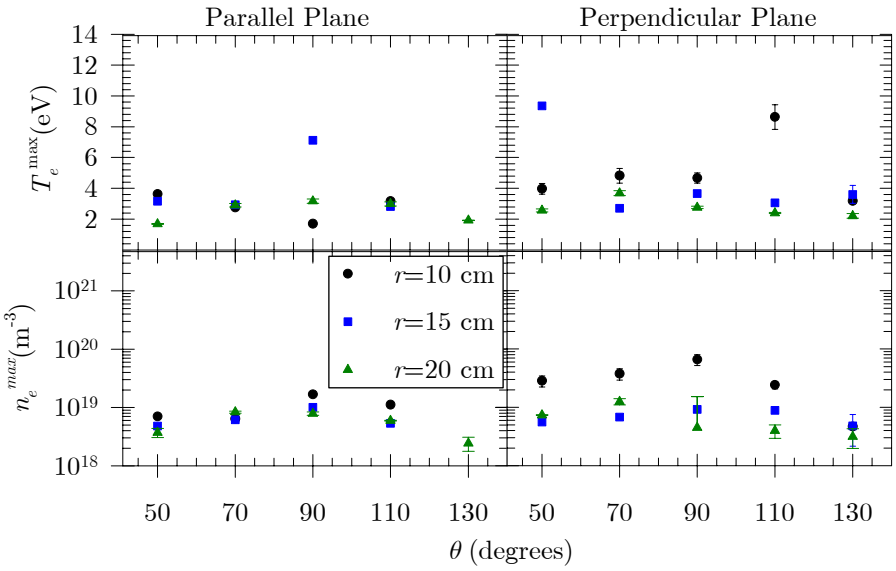

Figure 3.9 Maximum values of electron temperature and density as measured by the triple Langmuir probe in the plume of a 5-J laboratory PPT.

Figure 3.10 displays the peak values for electron temperature and number density for a 20-J laboratory PPT. This is presented in an identical fashion as that in Figure 3.9. The trends are similar to those in Figure 3.9 as well. The scatter on peak electron temperature values makes it difficult to identify any relationship with angle. On the whole the peak electron temperature values are elevated as compared to the 5-J data. The peak electron number density plots show a similar trend to the 5-J data with the exception of the magnitudes being significantly higher. The values still peak along the centerline

and decrease towards the off-axis angles. There is not as much delineation between the radial positions as existed in the 5-J results.

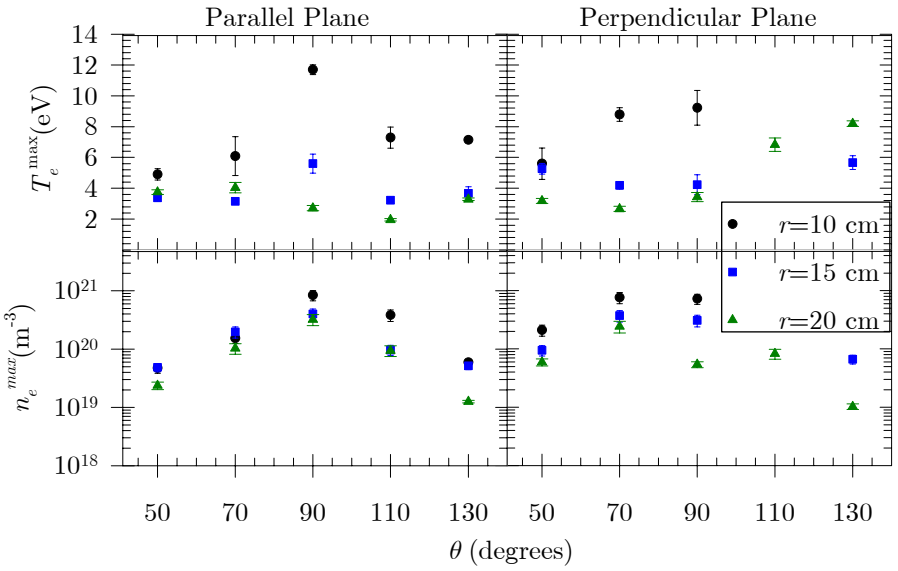

Figure 3.10 Maximum values of electron temperature and density as measured by the triple Langmuir probe in the plume of a 20-J laboratory PPT.

Figure 3.11 summarizes the peak values of electron temperature and number density of a 40-J laboratory PPT. This figure is laid out in an identical fashion as the previous two figures for the 5-J and 20-J results. Much more scatter exists in the peak electron temperature results in both measurement planes for the 40-J results. There still is not any easily identifiable trend here. Again the peak electron number density values exhibit a similar trend to the 5-J and 20-J data. The peak electron number density values have the appearance of flattening out in the off-axis areas at this energy level. This suggests that the plume is expanding more than at the two lower energy levels. The spatial discretization of the measurements does not allow an assessment of plume asymmetry at any of the energy levels.

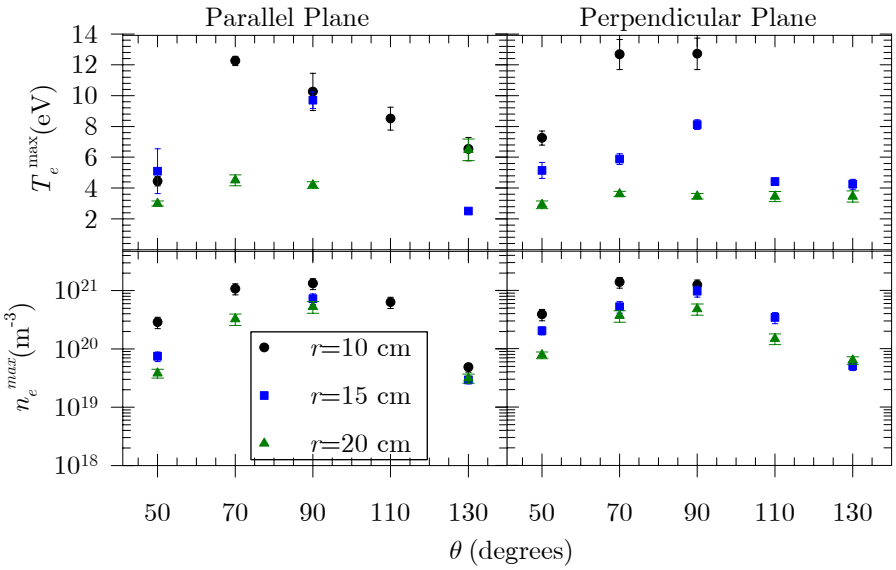

Figure 3.11 Maximum values of electron temperature and density as measured by the triple Langmuir probe in the plume of a 40-J laboratory PPT.

Figure 3.12 shows the influence discharge energy has on the axial dependence of the measurements. The maximum electron temperature and density is plotted as a function of axial distance from the Teflon® surface along the thruster centerline. Evident from the plot of maximum temperature is the fact that near the exit plane discharge energy plays a significant role in the maximum temperatures. The higher the discharge energy the higher the maximum electron temperature. As the probe is moved further downstream from the Teflon® surface, the temperatures quickly fall off and converge to a near common value.

The discharge energy clearly affects the maximum number densities. The higher the discharge energy is, the larger the density of the plume due to a greater mass of Teflon® being ablated. But the 5 and 20-J cases show that the maximum density falls

over an order of magnitude between 10 and 20 cm, while the 40-J data stays around 10^{21} m^{-3}.

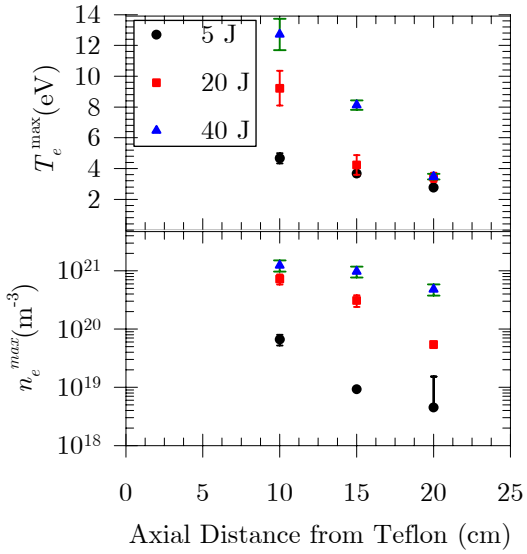

Figure 3.12 Spatial variation of maximum electron temperature and densities on the centerline of a laboratory PPT plume as a function of discharge energy.

These current results compare well with the previous work by Eckman, et al. (2001) on this same thruster using triple Langmuir probes in a voltage-mode. Those previous measurements used the voltage-mode method in which significant amounts of noise corrupted the voltage measurements while the arc was present. This was compensated for by employing a smoothing algorithm to remove the spikes in the initial portion of the pulse as well as the high-frequency noise or bit error over-laying the entire voltage measurement. This had the effect of reducing the peak values at the beginning of the pulse and perhaps creating an artificial shape to the ramp up of the electron temperature. In this thesis the results were portrayed as is without the use of smoothing algorithms that could possibly reduce the peak values. The electron number density

portion of Figure 3.12 compares well with the equivalent results by Eckman, et al. (2001). The trends were quite similar and the absolute magnitudes were agreeable.

These results also compare favorably to published results by Bushman, et al. (2001) using a quadruple Langmuir Probe on a coaxial Gasdynamic style PPT. They did not report peak electron temperatures as high as these, but they also were not able to reduce data within the PPT discharge. This was due to excess noise on their voltage measurements during the arc. From the time they begin acquiring reducible data it begins around 2 eV and tapers down logarithmically much like our results do in the period after the arc has ceased. No other known measurements have been taken of electron temperature in a PPT during the arc. This could be why previously reported peak electron temperature measurements have been considerably lower then the peak values reported within this thesis.

Chapter 4 Summary, Conclusions, and Recommendations

In this thesis a diagnostic technique was developed and applied to a pulsed plasma thruster in order to measure electron temperature and density of its exhaust plume. Triple and double Langmuir probes were used over a significant portion of the downstream exhaust plume of the PPT. The application of these probes to the unsteady PPT plasma is documented within this thesis to aid future work in this field. The results of this thesis are summarized below in detail along with recommendations for future work.

4.1 Summary of Experimental Setup, Diagnostics, and Procedures

Following in the footsteps of Eckman, et al. (2001) triple Langmuir probes were used on the plasma of a PPT. They were used to measure electron temperature and density of the plume. Improvements over the previous work included migrating the experiment into a much larger vacuum facility to mitigate any potential interactions with the tank walls. A new method for use of the triple probes was implemented. This was referred to as the current-based method. This new technique adapted for use within the unsteady plasma environment of the PPT was taken from Chen, et. al. (1965 and 1971). It eliminated all voltage measurements and instead used only current measurements. This technique proved to be much less susceptible to noise entering the system and corrupting the data.

A probe motion system was created to allow automated movements of the probes within the vacuum facility. The system allowed for translation from the thruster exit plane to greater than 20 cm downstream. The system also included a rotation stage to rotate the thruster itself a full 180°. This allowed for probe measurements in areas to either side of the thruster centerline. The probe motion system had a feature that allowed for the rotation of the probe itself with respect to the thruster. This feature was included to help identify or mitigate probe/flow misalignments. Unfortunately the motor used for this failed quite early in the testing before any useful information was obtained from its use. The entire probe motion system was controlled through a personal computer using visual basic programs to control the motion. This allowed for automation of the probe positions within the PPTs plume region.

To investigate any possible asymmetries in the PPT plume the thruster could be manually rotated 90° on the probe motion system. This allowed for the placement of the probes on two planes, perpendicular and parallel to the PPT electrodes.

Data was collected over a range of positions within the PPT plume. This included radial positions of 10, 15, and 20 cm downstream from the propellant surface. Data was collected 20° to either side of the thruster centerline at each of the radial positions. Data was also collected at these same locations with the PPT position in both mounting positions, parallel and perpendicular. All of this was repeated with the thruster operating at three different energy levels, 5, 20, and 40-J.

4.2 Summary of Data Reduction, Analysis, and Results

The collected data was reduced using an algorithm created in Fortran90 to take the raw probe current measurements and solve the triple Langmuir equations for electron

temperature and density. The algorithm used significantly improved on the algorithm used previously by Eckman et. al. (2001). It accounted for possible sheath interaction affects by implementing Laframboise's (1966) ion current collection theory. The inclusion of this new equation required the addition of a new equation solver in order to solve the resulting system of non-linear equations.

A full uncertainty analysis was performed on the full set of non-linear equations describing the triple Langmuir probe. Using known measurement uncertainties the algorithm calculates the absolute error for electron temperature and density. This provides a full set of error bars for all the reduced data based upon experimental uncertainties.

The full reduced data sets were presented in Figure 3.3-Figure 3.8. Plots showing the maximum values as a function of angular position within the PPT plume were presented in Figure 3.9-Figure 3.11.

4.3 Recommendations for Future Experiments

There are several recommendations to be made that if implemented could lead to more insight into the exhaust plume of a pulsed plasma thruster. These mainly fall into experimental improvements in the apparatus and technique.

- Improve Resolution of Current Probes

The current probes that were used had a minimum sensitivity of approximately 10 mA. During operation of the PPT at low energy levels and at positions well off of centerline and in the back flow regions the induced current in the triple Langmuir probes was quite small, on the order of the minimum sensitivity of the current probes and smaller. There are techniques that could be used to improve the sensitivity of these

devices to measure smaller currents. These probes are Hall Effect current probes and operate by sensing the induced magnetic field in a conductor. By increasing the number of turns this conductor makes while in the probe it can act to multiply the resolution. Though troublesome to make hundreds of turns of fine wire in the current probe it could improve the resolution of electron temperature and density in the backflow areas.

- Identify initial electron temperatures

The initial triple Langmuir probe signals are on the order of milliamps while the peak signals can be upwards of an amp. Having the range of resolution to cover both of these regimes may not be possible, but strictly focusing on the initial portion of the plume may be useful. Measurements of the plume could be done in a multipart process to piece together the entire time-dependent electron temperature of the plume at a particular location. Measurements of the initial portion of the plume could be done with techniques for measuring small currents with the use of filtering techniques to reduce some of the electromagnetic noise that is present during this period. The instrumentation may need sort of protection from the peak currents of the plume.

- Flow vector Analysis

A more robust implementation of the ability to rotate the probe axis with respect to the thruster axis could lead to detection of the plasma flow direction at different points in the plume. This would also improve measurement results as the triple Langmuir probes should be aligned with the direction of plasma flow.

- Improve Probe Biasing Circuitry

The bias voltage used for both the double and triple Langmuir probes was provided by common 9-V and D-cell type batteries. These batteries have a limited

amount of current capacity and can be stressed when the probes are used in the denser portions of the plume where current draw is at its highest. This could be overcome by using larger current capacity batteries such as car or motorcycle type 12-V batteries. Perhaps even the use of a very well isolated DC power supply. The fear in the past over using DC power supplies was the noise that they would introduce into the system. With the use of the current-based TLP method noise is not as much of an issue as with the voltage-based method. So this may be a viable alternative to attempt. Though the power supplies used would need to be able to respond to the discharge on the order of microseconds without a significant bias voltage drop.

- Time of Flight Measurements

By using multiple triple Langmuir probes time of flight measurements could be taken to develop velocities of the plasma. These measurements would prove useful in the modeling efforts.

- Energy Measurements

Measurements of ion energy in the plume of a PPT would be very useful for the WPI's modeling efforts as well for the electric propulsion community. This would be some sort of gridded energy analyzer such as an RPA. Keeping the grids from shorting to one another in the plume of a PPT would be a challenge. Perhaps a glow cleaning method could be used much like for the triple Langmuir probes to burn off any contaminants.

References

Antropov, N., Gomilka, L., Diakonov, G., Krivonosov, I., Popov, G., Orlov, M., "Parameters of Plasmoids Injected by PPT," 33rd Joint Propulsion Conference, Seattle, WA, July 6-9, 1997.

Arrington, L., and Haag, T., "Multi-Axis Thrust Measurements of the EO-1 Pulsed Plasma Thruster," AIAA Paper 99-2290, June 1999.

Arrington, L., Marrese, C., and Blandino, J., "Pulsed Plasma Thruster Plume Study: Symmetry and Impact on Spacecraft Surfaces," AIAA Paper 2000-3262, July 2000.

Benson, S., Arrington, L., Hoskins, A., Meckel, N., "Development of a PPT for the EO-1 Spacecraft," AIAA Paper 99-2276, June 1999.

Brill, Y., Eisner, A., and Osborn, L., "The Flight Application of a Pulsed Plasma Microthruster; the NOVA Satellite," AIAA Paper 82-1956, Nov 1982.

Bufton, S. A., Burton, R. L., and Krier, H., "Measured Plasma Properties at the Exit Plane of a 1 kW Arcjet," AIAA 95-3066, July 1995.

Burton, R., and Bushman, S., "Probe Measurements in a Coaxial Gas Dynamic PPT," AIAA Paper 99-2288, June 1999.

Bushman, S.S., and Burton, R.L., "Heating and Plasma Properties in a Coaxial Gasdynamic Pulsed Plasma Thruster," *AIAA Journal of Propulsion and Power*, Vol. 17, No. 5, 2001, pp. 959-966.

Byrne, L., Gatsonis, N.A., and Pencil, E.J., "Triple Langmuir Probe Measurements in the Plume and Backflow Region of a Pulsed Plasma Thruster", AIAA Paper 01-3640, July 2001.

Chen, S., "Studies of the Effect on Ion Current on Instantaneous Triple-Probe Measurements", *Journal of Applied Physics*, Vol. 42, No. 1, 1971, pp. 406-412.

Chen, S., and Sekiguchi, T., "Instantaneous Direct-Display System of Plasma Parameters by Means of Triple Probe", *Journal of Applied Physics*, Vol. 26, No 8, 1965, pp. 2363-2375.

Coleman, H.W. and Steele, W.G., *Experimentation and Uncertainty Analysis for Engineers*, John Wiley & Sons, 1999.

Chung, P.M., Talbot, L., and Touryan, K.L., *Electric Probes in Stationary and Flowing Plasmas*, Vol. 2, Springer-Verlag, New York, 1975, pp. 29-32.

Data Sheet for TCP-202 DC Coupled Current Probe, Tektronix Corporation, http://www.Tek.com.

Eckman, R. F., Byrne, L., Gatsonis, N. A., and Pencil, E. J., "Triple Langmuir Probe Measurements in the Plume of a Pulsed Plasma Thruster," *Journal of Propulsion and Power*, Vol. 17, No. 4, 2001, pp. 762-771.

Eckman, R., "Langmuir Probe Measurements in the Plume of a Pulsed Plasma Thruster," M.S. Thesis, Worcester Polytechnic Institute, Worcester, MA, February 1999.

Fife, M., "Hybrid-PIC Modeling and Electrostatic Probe Survey of Hall Thrusters," Ph.D. Dissertation, MIT, Cambridge, MA, 1998.

Gagne, M., "Experimental and Numerical Investigation of Pulsed Plasma Thruster Plumes," M.S. Thesis, Worcester Polytechnic Institute, January 2000.

Gallimore, A.D., Kell, A. J., and Jahn, R.G., "Anode Power Deposition in Quasi-Steady MPD Thusters," AIAA Paper 90-2668, 1990.

Gatsonis, N. A. and Yin, X., "Hybrid (Particle-Fluid) Modeling of Pulsed Plasma Thruster Plumes," *Journal of Propulsion and Power*, Vol. 17, No. 5., 2001, pp. 945-958.

Gatsonis, N. A., Eckman R., Yin, X., Pencil, E. J., and Myers, R. M., "Experimental Investigations and Numerical Modeling of Pulsed Plasma Thruster Plumes," *Journal of Spacecraft and Rockets*, Vol. 38, No. 3, 2001, pp. 454-464.

Gatsonis, N., and Yin, X., "Particle/Fluid Modeling of Pulsed Plasma Thruster Plumes," AIAA Paper 99-2299, June 1999.

Gatsonis, N.A., Zwahlen, J., and Wheelock, A., "Characterization of a Pulsed Plasma Thruster Plume Using a Quadruple Langmuir Probe Method," AIAA Paper 2002-4123, July 2002.

Guman, W. J., and Begun, M., "Exhaust Plume Studies of a Pulsed Plasma Thruster," AIAA Paper 97-704, April 1978.

Guman, W. J., and Nathanson, D. M., "Pulsed Plasma Microthruster Propulsion System for Synchronous Orbit Satellite," *Journal of Spacecraft and Rockets*, Vol. 7, No. 4, 1970, p. 409.

Guman, W. J., and Begun, M., "Pulsed Plasma Plume Studies," Air Force Rocket Propulsion Laboratory Report, AFRPL-TR-77-2, March 1977.

Hammel, J., Krumanaker, and M., Zwahlen, J., "Design and Construction of an Experimental Setup for Plume measurements in a Large Vacuum Facility," Major

Qualifying Project ME-NAG-9901, Worcester Polytechnic Institute, Worcester, MA, October 1999.

Hirata, M., and Murakami, H., "Exhaust Gas Analysis of a Pulsed Plasma Engine," IEPC Paper 84-52, Tokyo, Japan, 1984.

Johnson, E.O. and Malter, L., *Physical Review*, Vol. 80, 1950.

Laframboise, J., "Theory of Cylindrical and Spherical Langmuir Probes in a Collisionless Plasma at Rest," UTIAS Rept. 100, June 1966.

Lieberman, M.A., Lichtenberg, A.J., *Principles of Plasma Discharges and Materials Processing*, John Wiley & Sons, 1994.

Markusic, T. E., and Spores, R. A., "Spectroscopic Emission Measurements of a Pulsed Plasma Thruster Plume," AIAA Paper 97-2924, July 1997.

Meckel, N., Hoskins, A., Cassady, R., Myers, R., Oleson, S., and McGuire, M., "Improved Pulsed Plasma Thruster Systems for Satellite Propulsion," AIAA Paper 96-2735, July 1996.

Mitchner, M., and Kruger, C.H., *Partially Ionized Gases*, John Wiley & Sons, 1973.

Myers, R., Arrington, L., and Pencil, E., Carter, J., Heminger, J, and Gatsonis, N., "Pulsed Plasma Thruster Contamination," AIAA Paper 96-2729, July 1996.

Myers, R., Oleson, S., Curran, F., and Schneider, S., "Small Satellite Propulsion Options," AIAA Paper 94-2997, August 1994.

Peterson, E. W., and Talbot, L., "Collisionless Electrostatic Single-Probe and Double-Probe Measurements," *AIAA Journal*, Vol. 8, No.12, 1970, pp.2215-2219.

Press, W.H., Teukolsky, S.A., Vetterling, W.T., and Flannery, B.P., *Numerical Recipes in Fortran 77: The Art of Scientific Computing*, 2nd ed., Vol. 1, Cambridge University Press, 1992.

Press, W.H., Teukolsky, S.A., Vetterling, W.T., and Flannery, B.P., *Numerical Recipes in Fortran 90: The Art of Parallel Scientific Computing*, 2nd ed., Vol. 2, Cambridge University Press, 1996.

Rudolph, L.K., Harstad, K.G., Pless, L.C., and Jones, R.M., "Plume Characterization of a One-Millipound Solid Teflon Pulsed Plasma Thruster," Air Force Rocket Propulsion Laboratory TR-79-60, NASA CR-162786, Sept. 1979.

Sackheim, R., and Byers, D., "Status and issues Related to In-Space Propulsion Systems," *Journal of Propulsion and Power*, Vol. 14, No. 5, 1998.

Sankovic, J., and Duning, J., "NASA's Electric Propulsion Program," AIAA Paper 99-2161, June 1999.

Schott, L., "Electrical Probes," *Plasma Diagnostics*, edited by W. Lochte-Holtgreven, North –Holland Publishing Company, Amsterdam, 1968.

Spanjers, G. G., Malak, J. B., Leiweke, R. L., and Spores, R. A., "The Effect of Propellant Temperature on Efficiency in the Pulsed Plasma Thruster," AIAA Paper 97-2920, July 1997.

Spanjers, G.G., Antonsen, E.L., Burton, R.L., Keidar, M., Boyd, I.D., and Bushman, S.S., "Advanced Diagnostics for Millimeter-Scale Micro Pulsed Plasma Thrusters," AIAA Paper 2002-2119, May 2002.

Spanjers, G.G., Lotspeich, J.S., McFall, K.A., and Spores, R.A., "Propellant losses Because of Particulate Emission in a Pulsed Plasma Thruster," *Journal of Propulsion and Power*, Vol.14, No.4, 1998, pp. 554-559.

Spores, R., and Birkan, M., "The USAF Electric Propulsion Program," AIAA Paper 99-2162, June 1999.

Thomassen, K. I., and Tong, G., "Interferometric Density Measurements in the Arc of a Pulsed Plasma Thruster," *Journal of Spacecraft and Rockets*, Vol. 10, No. 3, March 1973, pp. 163-164.

Thomassen, K. I., and Vondra, R.J., "Exhaust Velocity Studies of a Solid Teflon Pulsed Plasma Thruster," *Journal of Spacecraft and Rockets*, Vol. 9, No. 1, Jan. 1972, pp. 61-64.

Tilley, D. L., Kelly, A. J., and Jahn, R. G., "The Application of the Triple Probe Method to MPD Thruster Plumes," AIAA 90-2667, July 1990.

Vondra, R. J., Thomassen, K., and Solbes, A., "Analysis of Solid Teflon Pulsed Plasma Thruster," *Journal of Spacecraft and Rockets*, Vol. 7, No. 12, 1970, pp. 1402-1406.

Zakrzwski, C., Sanneman, P., Hunt, T., Blackman, K., "Design of the EO-1 Pulsed Plasma Thruster Attitude Control Experiment," AIAA Paper 2001-3637, July 2001.

Zakrzwski, C., Benson, S., Sanneman, P., Hoskins, A., "On-Orbit Testing of the EO-1 Pulsed Plasma Thruster," AIAA Paper 2002-3973, July 2002.